Journal of Hazardous Materials 498 (2025) 139933

Contents lists available at ScienceDirect

Journal of Hazardous Materials

journal homepage: www.elsevier.com/locate/jhazmat

Sunlight driven photo-treatment of polyhydroxybutyrate microplastics mediated by carbon nanodots-doped ZnO mesocrystals: Induced surface changes boost degradation in soil and biofilm formation

Simone Russo [a,b], Marica Muscetta [a,*], Immacolata Liotta [a,c], Moreno Rizzo [a], Daniele Marra [a], Gennaro Gentile [c], Beate Förster [d], Sergio Caserta [a,e,f], Raffaele Marotta [a,c], Mariacristina Cocca [c], Giuseppe Vitiello [a,b,c,**]

[a] Department of Chemical, Materials and Production Engineering (DICMaPI), University of Naples Federico II, Piazzale V. Tecchio 80, Naples 80125, Italy
[b] CSGI, Center for Colloid and Surface Science, via della Lastruccia 3, Sesto Fiorentino, FI, Italy
[c] Institute for Polymers, Composites and Biomaterials (IPCB), National Research Council (CNR) of Italy, Via Campi Flegrei, 34, Pozzuoli, NA 80078, Italy
[d] Ernst Ruska-Centre for Microscopy and Spectroscopy with Electrons, Physics of Nanoscale Systems (ER-C-1), Forschungszentrum Jülich, Wilhelm-Johnen-Straße, Jülich, Germany
[e] CEINGE, Biotecnologie Avanzate Franco Salvatore, Via Gaetano Salvatore, Napoli 486 - 80145, Italy
[f] Consorzio Interuniversitario Nazionale per la Scienza e Tecnologia dei Materiali (INSTM), UdR INSTM Napoli Federico II, P.le Ascarelli 80, Napoli 80125, Italy

HIGHLIGHTS

- A bottom-up strategy leads to ZnO mesocrystals doped with carbon nanodots (CNDs).
- Biowaste-derived molecules are valorized into photoactive nanomaterials.
- CNDs/ZnO mesocrystals enhance PHB microplastics (MPs) sunlight-driven photo-oxidation.
- The photoinduced modifications of MPs surface favor the biodegradation process.
- The photochemical treatment improve the microbial adhesion onto MPs.

GRAPHICAL ABSTRACT

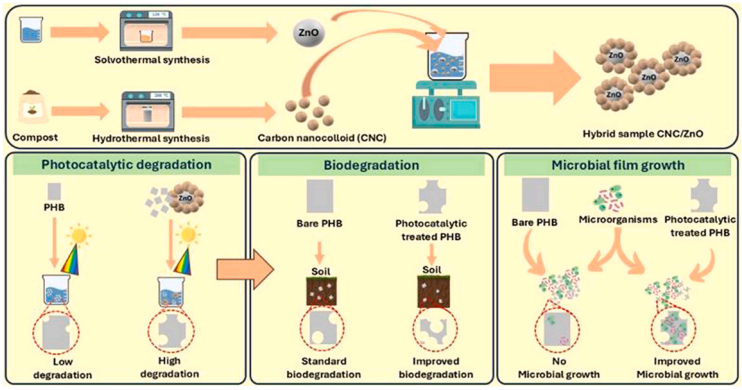

ARTICLE INFO

Keywords:
Carbon nanodots
ZnO
Microplastics
Photocatalysis

ABSTRACT

Plastics are widely used due to their versatility. However, their accumulation as microplastics and nanoplastics in the environment poses a significant threat for the ecosystems. Although biodegradable polymers, like polyhydroxybutyrate (PHB), offer a sustainable alternative, their degradation could still lead to fragmentation and MP accumulation, hence it is essential to enhance biodegradation rates in order to mitigate environmental

* Corresponding author.
** Corresponding author at: Department of Chemical, Materials and Production Engineering (DICMaPI), University of Naples Federico II, Piazzale V. Tecchio 80, Naples 80125, Italy.
E-mail addresses: marica.muscetta@unina.it (M. Muscetta), giuseppe.vitiello@unina.it (G. Vitiello).

https://doi.org/10.1016/j.jhazmat.2025.139933
Received 23 June 2025; Received in revised form 4 August 2025; Accepted 19 September 2025
Available online 20 September 2025

Biodegradation
Biofilm

impacts. This study investigates the integration of photocatalytic pretreatment with natural biodegradation to accelerate PHB biodegradation. Photoactive ZnO mesocrystals doped with biowaste-derived carbon nanodots, prepared via a wet-chemical approach, are proposed to improve the photocatalytic efficiency under sunlight. ZnO mesocrystals doped with 30 wt% of carbon nanodots exhibited superior photocatalytic properties, thus photodegrading PHB microplastics more efficiently than bare ZnO. Phototreated PHB microplastics exhibit an improved biodegradation in soil when exposed for a controlled irradiation time. Additionally, PHB microplastics photo-treated in the presence of doped mesocrystals showed an enhanced microbial colonization indicating improved biofilm formation. These findings highlight the potential of photocatalytic pretreatment in modifying surface properties to boost degradation in soil, thus offering a promising strategy for reducing microplastic accumulation.

1. Introduction

Plastics are widely used due to their numerous advantages, such as light weight, good stiffness, effective insulation and high resistance to corrosion [1–3]. These materials are used in many different applications like coating, insulation, construction, painting and electronics [4–6]. Global plastic production has surged from 1.5 million metric tons in 1950 to a staggering 390.7 million metric tons in 2021 with plastic waste predicted to increase by approximately 250 million metric tons by 2025 [7,8]. As plastic materials are released into the environment, they degrade and fragment into microplastics (MPs), ranging in size from 5 mm to 100 nm, and nanoplastics (NPs), with size smaller than 100 nm [9,10], which pose a serious threat to living organism by inhibiting their growth, development and reproduction [11,12]. Furthermore, MPs and NPs can enter the food chain, impacting marine environment across trophic levels including planktonic species, invertebrates and vertebrates, fish and crustaceans [13], ultimately affecting human health [14]. Exposure to NPs and MPs has been potentially linked to various health concerns, such as cancer, respiratory disorders, and chronic inflammation [15].

Various techniques, such as coagulation, adsorption and chemical oxidation, are used to remove MPs from the environment, but these techniques have different drawbacks [9]. Adsorption and chemical oxidation face the challenge that the reusability and cost-effectiveness of the adsorbent or catalyst are critical factors in determining their viability and large-scale application [16]. On the other hand, coagulation is a method in which MPs are not mineralized but only relocated from one phase, water, to another, sludge with implication also for agri-food sectors if sludge are applied. Meaning that the pollution associated with MPs intensifies, and the objective to restore the environment is delayed [17]. To address the issue, the use of biodegradable polymers is considered a preferable alternative to non-biodegradable plastics [18]. Largely commercialized biodegradable plastics are polyesters, including polylactic acid (PLA), poly(ε-caprolactone) (PCL), and polyhydroxybutyrate (PHB) [19,20] due to the presence of ester bonds which can be hydrolyzed by natural enzymes. For example, PHB is easily attached by microorganisms, facilitating its uncomplicated biodegradation in soil and aquatic habitat [21–23]. Despite these advantages, the natural decomposition of PHB, can result in MPs accumulation, which serve as carriers for hazardous compounds that affect soil and aquatic species, as well as human health [21,24–26]. Therefore, a promising strategy could be represented by boosting the rate of biodegradation in order to reduce the accumulation of MPs in the environment. However, the chemical composition and morphology of MPs play a crucial role in their biodegradation [27]. Consequently, the adoption of pretreatment methods that modify crystallinity, surface roughness, and hydrophobicity may promote the initial microbial attachment to the plastic substrate, as fundamental stage in biofilm formation, and enhance the biodegradation process [28].

In this context, the integration of photochemical degradation of MPs with natural biodegradation processes should represent a valid opportunity, above all by exploiting the natural light. Photocatalysis is an eco-friendly technique that utilizes light irradiation to generate electron-hole pairs in semiconductors [29]. These charge carriers produce Reactive Oxygen Species (ROS) [30] that mineralize the organic substances [31]. Metal oxide semiconductors, like TiO_2, ZnO, CuO and CeO_2, are widely used for the photocatalytic degradation of dyes, pesticides, drugs and, more recently, microplastics [32–34]. Among them, zinc oxide exhibits chemical stability, excellent electron exchange and biocompatibility [35,36] which make it valuable for eco-sustainable uses. However, its moderately high bandgap (3.27 eV) limits its activity to UVA range and rapid charge recombination reduces its efficiency. An efficient way to overcome these limitations is represented by doping that is a technique commonly used to vary the number of electrons and holes in semiconductors. Among the several commonly used doping agents, carbon nanodots (CNDs) represent a valuable alternative because of the possibility to produce them by ecofriendly processes also starting by molecules deriving from biowastes. CNDs are carbonaceous nanoparticles with a diameter lower than 10 nm and exhibit excellent optical properties, including fluorescence, up-conversion photoluminescence and enhanced electron transfer [37,38] than, if combined by doping to semiconductors like ZnO, can improve the light utilization and the charges separation, thus enhancing photocatalytic activity [39].

In the present study, photoactive ZnO mesocrystals doped with biowaste-derived carbon nanodots are synthesized through a bottom-up wet-chemical route by varying the carbon content with the aim of optimizing photocatalytic degradation efficiency toward polyhydroxybutyrate (PHB) microplastics under sunlight irradiation. Rather than proposing photocatalysis as a field-remediation strategy, the photocatalytic treatment is here adopted as a surface modification tool to investigate the influence of photochemical handling on subsequent microbial biodegradation. Indeed, PHB microplastics are then subjected to degradation in soil and biofilm formation tests to examine the influence of photocatalytic pretreatment on the degradation process as well as biofilm adhesion and growth in order to gain deeper insight into the factors and conditions contributing to the enhanced degradation in soil. Definitely, this study highlights the chance of a biowaste valorization for producing functional materials with advanced photoactivity that can be exploited in designing biodegradable plastic supplies embedded with eco-inspired photocatalytic agents, thus enabling natural light-driven degradation and reducing the environmental persistence of microplastics.

2. Material and methods

2.1. Materials

Ethanol (EtOH, purity ≥ 99.8 %), triethylamine (TEA purity ≥ 99.8 %), zinc acetate dihydrate (ZnAc purity ≥ 99.8 %), glycerol (purity ≥ 99.8 %) reagents and Luria-Bertani (LB) broth were obtained by Sigma-Aldrich (Milan, Italy) and were used without further purification. Agri-food compost was furnished by Verde Vita S.r.l company (Alghero, Sardinia, Italy) and used by following the procedure reported in SI section. Polyhydroxybutyrate (PHB, Biomer T19, $M_w = 223$ kDa, $M_w/M_n = 1.23$) was supplied from Biomer (Germany) and dried under vacuum for 24 h at 40 °C to prevent hydrolysis during molding. After drying, 300 μm thick PHB films were prepared through compression molding at 175 °C under a pressure of 200 bar, followed by quenching to room

temperature using water-circulating cooling plates. Small PHB samples (4.5 mm×4.5 mm, 300 μm thick) were prepared as models of MPs for photocatalytic and degradation in soil tests. The soil used for the experiments was Valcofert S.R.L. universal soil (Empoli), with the following characteristics: 4.0 % organic carbon (SS), an electric conductivity of 1.0 dS/m, a dry bulk density of 950.0 kg/m^2, a total porosity of 85.0 % (v/v), and a pH of 7.0. *Pseudomonas fluorescens* SBW25 and *Bacillus subtilis* ND med strains were furnished by Micalis Institute, joint research unit of INRAE, AgroParisTech and University of Paris-Saclay, AgroParisTech (France).

2.2. Synthesis of carbon nanodots-doped ZnO mesocrystals

ZnO mesocrystals doped with bioderived CNDs were obtained by an impregnation method starting from specific amount of both the bare CNDs and ZnO particles. Firstly, CNDs were produced utilizing a hydrothermal technique using humic substances (HS) as carbon source. An aqueous solution of HS was prepared with a concentration of $8.9{\cdot}10^{-3}$ g·mL^{-1} in a final volume of 62.5 mL. The mixture was thoroughly stirred using a magnetic stirrer to ensure full dispersion maintaining the temperature at (25 ± 3) ºC and the pH to a value of about 7.0. Then, the solution was transferred into a stainless-steel autoclave lined with Teflon and then heated up to a temperature of 200 °C for 24 h. Afterwards, the mixture was subjected to centrifugation at a speed of 11500 rpm for two cycles, each lasting 7 min. The supernatant after centrifugation was retained and subjected to ultrasonic treatment for 5 min by using a tip-sonicator at a 40 % amplitude and filtration using a filter with a porosity of 0.22 μm. The CNDs obtained were collected in suspension with a concentration of 5 mg·mL^{-1}. Successively, bare ZnO crystals were synthetized following the protocol as previously described [40]. A brief description of the protocol is reported in **Section 1.2** of the SI. The ZnO mesocrystals were collected as a suspension with a concentration of 6 mg·mL^{-1}. CNDs-doped/ZnO mesocrystals were prepared by mixing specific amounts of CNDs and ZnO mixtures, which were sonicated appropriately to ensure proper dispersion. Hybrid samples were obtained with three different CNDs-doping contents corresponding to CNDs/ZnO weight ratios of 0.1, 0.3 and 0.6. Each hybrid suspension was gently stirred onto a magnetic stirrer for 24 h at 25 °C and at a pH 7. Finally, the samples were dried at 80 °C to obtain powdered samples for physicochemical characterization and functional tests. Hereafter, the obtained samples will be referred to as CNDs/ZnO-0.1, CNDs/ZnO-0.3, and CNDs/ZnO-0.6 respectively.

2.3. Physicochemical characterization of doped materials

Bare ZnO, CNDs and hybrid CNDs/ZnO mesocrystals, as well as PHB microplastic samples before and after the photodegradation, were analyzed for their physicochemical properties using a combination of techniques. Transmission Electron Microscopy (TEM) and Scanning Electron Microscopy (SEM) were used to characterize the morphological features of particles and PHB MPs. X-Ray Diffraction (XRD) was employed in order to investigate the graphitic nature of CNDs and the properties and crystalline structure of bare and hybrid mesocrystals, and to determine the crystalline index of PHB. Diffuse-Reflectance UV–vis (DRUV) and Photoluminescence (PL) measurements were performed on dry powder samples to study the optical properties of CNDs/ZnO mesocrystals and their changes with respect to bare ZnO and CNDs. Furthermore, Fourier Transform Infrared Spectroscopy with Attenuated Total Reflection (FTIR/ATR) was used to examine the surface chemistry of particles, and to monitor the chemical and structural changes in PHB MPs during both the photocatalytic degradation and degradation in soil. Further details on the analytical instruments and procedures used for the physicochemical characterization are provided in **Section 1.3** of SI.

2.4. Photocatalytic degradation of PHB microplastics via solar light

Photodegradation experiments were carried out on PHB MPs (4.5 mm × 4.5 mm) and five set of conditions were defined and summarized as follows:

- **Blank:** PHB + H_2O
- **Suspension 1:** PHB + H_2O + ZnO
- **Suspension 2:** PHB + H_2O + CNDs/ZnO-0.1
- **Suspension 3:** PHB + H_2O + CNDs/ZnO-0.3
- **Suspension 4:** PHB + H_2O + CNDs/ZnO-0.6

For each condition, five samples of PHB MPs were immersed in 20 mL of bi-distilled water placed into test tubes of 50 mL in volume and, alternatively, containing 20 mg of each type of photocatalyst. A blank solution was also prepared by immersing PHB samples in bi-distilled water in the absence of any catalyst. The photocatalytic degradation processes were carried out exposing the aqueous mixtures to solar light in Naples (40° 49' 25.91" N 14° 11' 34.134" E) from May to December. In order to obtain comparable results, the effect of MPs' photodegradation was analysed considering both time and accumulated energy per unit volume, Q_{UV}:

$$Q_{UV,n} = Q_{UV,n-1} + I * \frac{A}{V} * \Delta t; \Delta t = t_n - t_{n-1} \quad (1)$$

where I is the local solarirradiance [J·(h·cm^2)$^{-1}$], A is the irradiated surface [cm^2], V indicates the volume of reactor [cm^3], Δt represents the time interval [h] and Q_{UV}= is the accumulated energy per unit volume [J·cm^{-3}] [41]. The irradiance values, which were obtained from the NASA website (https://power.larc.nasa.gov/data-access-viewer/), were used to calculate Q_{UV} for samples exposed to solar radiation. In this situation, the spectrum being evaluated spans from 300 nm to 3000 nm. The activity of mesocrystals was restricted to UVA light irradiation due to their bandgap; therefore only the UVA component, which accounts for 4 % of the total irradiance, was considered in this study [42]. All details regarding the protocol adopted to calculate Q_{UV} was previously reported [43]. Specifically, the effect of the sunlight-driven photodegradation on PHB MPs in the presence of bare ZnO and CNDs-doped ZnO mesocrystals was analyzed after 61 hrs (Q_{UV}= 564.08 J·cm^{-3}) and 264 hrs (Q_{UV}= 2176.26 J·cm^{-3}). Photodegradation analysis of PHB microplastics (MPs) was performed in triplicate to determine the average degradation rate. For each experimental set, 12 MPs samples were used. At each sampling point, 4 MPs samples were collected and analyzed, with three different points measured on each MPs to obtain an average characterization.

2.5. Degradation in soil tests

PHB MPs both before and after the solar-driven photo-treatments, were subjected to degradation testing within soil burial. Each sample was carefully, dried, weighed and placed inside a metal mesh to ensure the retention of any fragments generated during the photodegradation process. These mesh-enclosed samples were then buried in soil, maintaining a spacing of approximately one centimeter between each sample and a burial depth of 3.0 cm as illustrated in Figure S1. The degradation of PHB samples in soil was monitored over a period of 135 days, with samples being recovered and analyzed after 15, 37, 62, 92 and 135 days of burial at a controlled temperature. Unburied PHB samples were analyzed for comparison too. The mesh size of the net used in the present work was 1.8 mm, 1.3 mm along the two orthogonal directions favoring a more intimate contact between the film surface and soil and reducing the extent of the eventual delay in the polymer degradation. In any case, the net was considered to equally influence the degradation of all the analyzed samples, thus allowing the evaluation of the degradation behavior of the materials and the comparison of the results.

Furthermore, FTIR and DSC analyses were carried out to monitor the chemical and structural changes in PHB MPs during both photocatalytic- and bio-degradation processes. Details on the physicochemical characterization are described in **Section 1.5** of SI section. The degradation of the tested PHB MPs was assessed using a gravimetric method determining the weight loss of the samples according to Eq. 2

$$WL(\%) = \frac{Wt_{t0} - Wt_{ti}}{Wt_{t0}} \times 100 \quad (2)$$

where Wt_{ti} is the weight of the sample after a certain burial time and Wt_{t0} is the weight before the burial. The crystallinity of the samples was calculated using the melting enthalpy of the fully crystalline PHB (145.0 $J \cdot g^{-1}$) [44]. The tests on PHB MPs were performed in triplicate.

2.6. Biofilm formation tests

Untreated and treated PHB MPs samples were contaminated by placing them in a nutrient broth containing *Pseudomonas fluorescens* SBW25 and *Bacillus subtilis* ND med strains, selected as high biofilm forming models [45]. In particular, the samples were separately exposed to *P. fluorescens* SBW25 and *B. subtilis* NDmed cultures for 72 h of growth in static conditions. All experiments were performed in triplicate for each sample and for both microorganisms. Specifically, frozen glycerol stock solution (25 v/v %) of both microorganisms, stored at −80 °C, were plated on LB agar (10.0 $g \cdot L^{-1}$ tryptone, 5.0 $g \cdot L^{-1}$ yeast extract, 5.0 $g \cdot L^{-1}$ NaCl, 15.0 $g \cdot L^{-1}$ agar, bi-distilled water) and incubated overnight respectively at 28 °C and 30 °C. Single colonies were then picked, resuspended in fresh LB broth (10.0 $g \cdot L^{-1}$ tryptone, 5.0 $g \cdot L^{-1}$ yeast extract, 5.0 $g \cdot L^{-1}$ NaCl) and incubated overnight under shaking (150 rpm) at the same temperatures. The optical density, measured at 600 nm ($OD_{600\ nm}$), of the suspension was analysed, and precise dilution in fresh medium was performed to achieve the chosen initial $OD_{600\ nm}$ value of 0.1. For biofilm formation, a proper volume (2.0 mL) of each bacterial suspension was inoculated in a Petri dish (45 mm) and the MP coupons were singularly inserted into and gently agitated with a loop to ensure the suspension. The Petri dishes were then incubated at 30 °C without shaking for 72 h.

After incubation, the coupons were carefully removed from the Petri dishes and transferred upside-down on glass slides for staining and imaging. The staining and imaging protocol was adapted from a previously described method [46]. Specifically, working in a dark room, a proper volume (100 µL) of staining solution was dropped on each sample. The staining solution was prepared by adding 3.0 µL of SYTO9 and 3.0 µL of propidium iodide in bi-distilled water (1 mL). After 30 min at room temperature, the stained coupons were analysed using a Confocal Laser Scanning Microscopy (CLSM 510META, Zeiss) equipped with an argon laser (LASOS Lasertechnik GmbH, LGK 7812 ML4) and two helium/neon laser (LASOS Lasertechnik GmbH, LGK 7628–1 and LGK 7786 P).

Experimental observations were performed with a Plan Apo λ 63 X/1.4 NA oil-immersion objective and a Zeiss digital camera, with a standard field of view of 1024 pixels x 1024 pixels, corresponding to 142.8 µm x 142.8 µm. Excitation was provided at a wavelength of 488.6 nm using a detection filter of 498 nm and at a wavelength of 561.5 nm with a detection filter of 580 nm. 3D Images were acquired applying Z-stacks along the biofilm thickness using a 0.6 µm interval between consecutive layers. Image processing was performed for each single field of view acquired using BiofilmQ through MATLAB© [47]. BiofilmQ allows the analysis of Z-stack images by denoising and segmenting images with customized settings and by declumping into voxels of preferred dimensions. Single cells voxel analyses are performed to obtain several parameters. Settings for denoising were chosen according to previous campaigns of biofilm visualization: convolution kernel size xy = 5, z = 3; medium filter along Z selected; top-hat filtering with size 25 voxels (3.49 µm). Segmentation was performed with the Otsu method with 3 classes, with class 2 assigned to background and a sensitivity of 0.4 (sensitivity was chosen by comparing different image analyses with different values), and objects were declumped with cube size of 20 voxels (2.80 µm cube side length). Both green (live) and red (dead) channels were processed, and after segmentation, the two channels were merged. Biofilm thickness, biovolume, and substratum coverage were selected as key parameters for analysis.

3. Results and discussion

3.1. Physicochemical features of synthetized CNDs/ZnO mesocrystals

TEM and SEM images of hybrid CNDs/ZnO mesocrystals compared to bare ZnO ones and CNDs are shown in Fig. 1. Bare ZnO exhibited a hexagonal shape with an average diameter of 5.0 ± 1.5 μm, resulting from the aggregation of smaller primary particles into mesocrystals (Fig. 1A). SEM images revealed a truncated pseudo-hexagonal pyramid shape (Fig. 1D). In contrast, CNDs distinctly exhibited a significantly smaller average diameter of 6.0 ± 3.0 nm (Figs. 1B and 1E), thus highlighting their nanoscale size if compared to ZnO mesocrystals. As shown in Figs. 1C and 1F, hybrid CNDs/ZnO-0.3 mesocrystals (reported as reference) displayed an average size of 180 ± 55 nm with a pseudo-hexagonal shape though less regular than that of bare ZnO mesocrystals. The presence of CNDs on ZnO surface was highlighted by the shadow surrounding the mesocrystals. These morphological differences were due to the influence of CNDs during the preparation which limited ZnO crystals aggregation, whose structure was probably altered by the tip-sonication performed to favor the re-suspension in aqueous medium before CNDs functionalization. This step probably contributed to the breakup of larger ZnO particles and enhanced their integration within the CND matrix and making them less distinguishable in the final morphology.

The surface doping of ZnO mesocrystals with bioderived CNDs and its effect on the crystalline structure were assessed by FTIR and XRD analyses, respectively, as shown in Fig. 2. The FTIR spectra of CNDs/ZnO confirmed that the protocol adopted was successful (Fig. 2A). Specifically, hybrid mesocrystals exhibited a distinct Zn-O vibrational peak at 450 cm^{-1} [48]. Notably, a significant shift in the Zn-O characteristic vibrational peak from 449 cm^{-1} for pure ZnO to 432 cm^{-1} in the doped materials was detected. This shift may result from the interaction between the functional groups of CNDs and Zn^{2+} ions, potentially forming a complex between the carbon nanodots and zinc ions and thereby the vibrational properties. The incorporation of CNDs was further supported by the presence of a more intense and broader band around 3340 cm^{-1}, corresponding to O-H stretching vibrations (Fig. 2B) [49]. Additionally, the peaks near 1590 cm^{-1} and 1415 cm^{-1} , attributed to C═C stretching and C-H bending vibrations, respectively, exhibited increased intensities too [50,51]. These peaks also appeared in the spectra of bare ZnO, likely originating from adsorbed water and residual unreacted organic compounds used in the synthesis [52]. However, they were likewise characteristic of carbon nanodots, reflecting their functional groups and carbonaceous structure [49,53]. Consequently, the hybrid samples exhibited higher transmittance intensities for these vibrational modes. It is important to note that the C═C stretching observed in the CNDs spectrum (Fig. 2B) indicates the presence of sp^2-hybridized carbon, suggesting that the CNDs contain both sp^2 and sp^3 hybridizations [54]. Another significant observation derived from the FTIR spectrum analysis was its resemblance to that of humic substances, as shown in Figure S3, suggesting that hydrothermal treatment did not significantly alter the primary functional groups of the precursor.

XRD spectra of CNDs-doped/ZnO mesocrystals (Fig. 2C) indicated that all samples exhibited the characteristic hexagonal crystalline structure of wurtzite, as evidenced by the comparison with bare ZnO [55,56]. In contrast, the XRD spectrum of CNDs (Fig. 2C and S4) revealed an amorphous nature as indicated by the presence of a broad band at 2θ= 24.8°, which is ascribable to the C(002) plane typical of graphitic carbon dots [57,58]. Although CNDs exhibited an amorphous structure similar to their humic substance (HS) precursor (Figure S4),

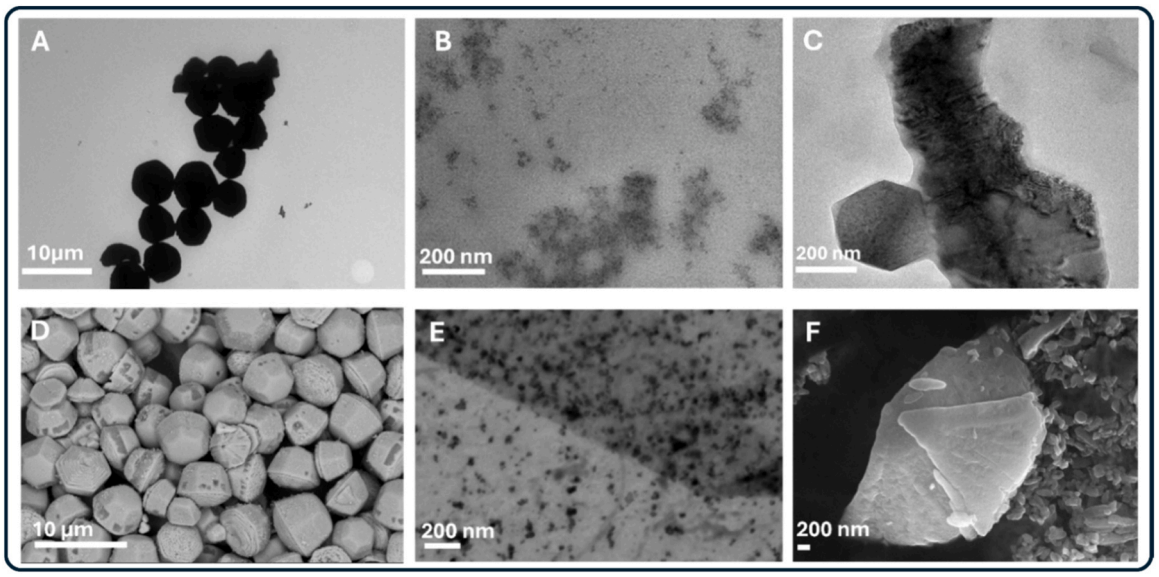

Fig. 1. TEM and SEM images of bare ZnO (A,D), bare, CNDs (B,E) and CNDs/ZnO-0.3 (C,F) respectively.

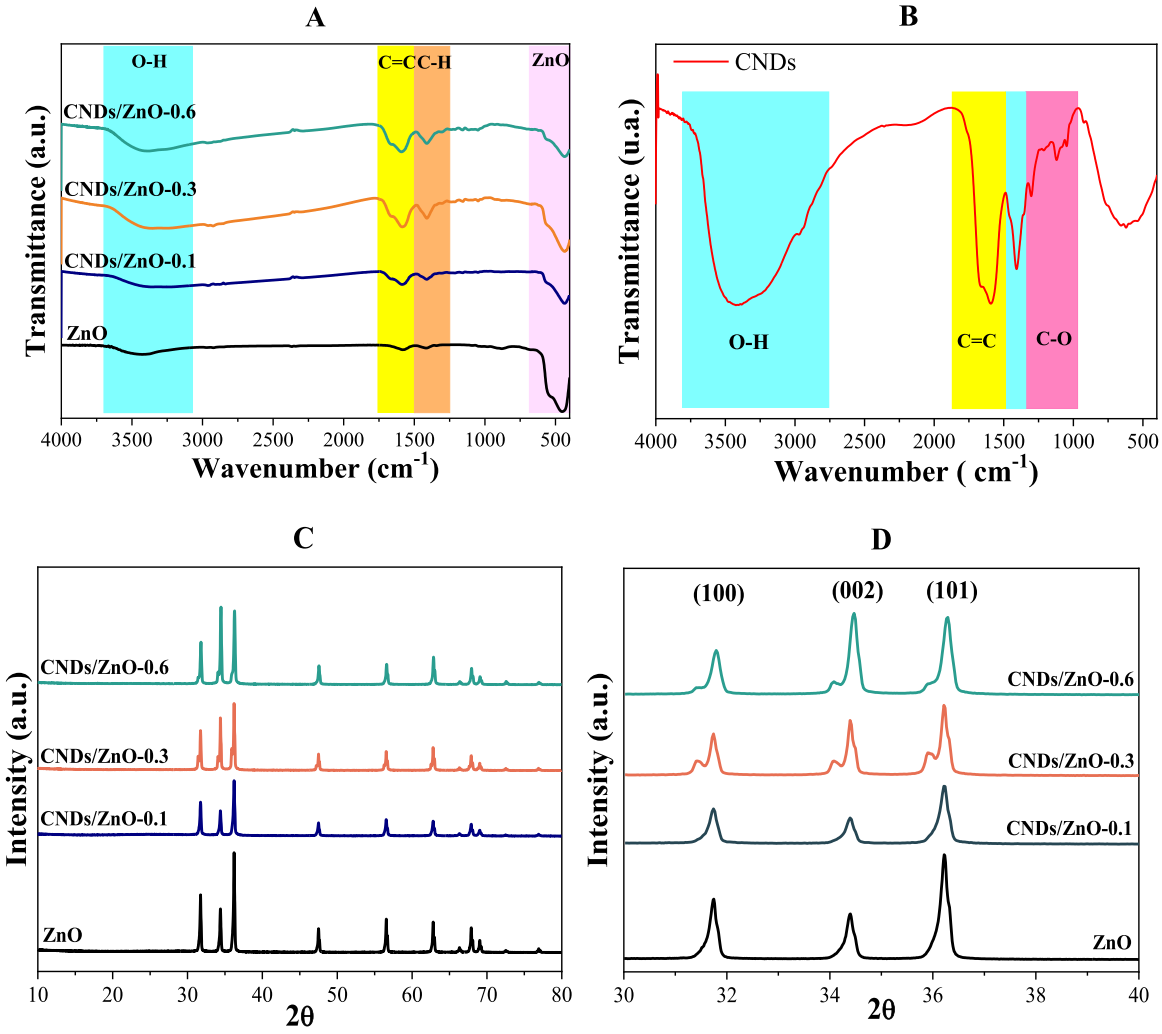

Fig. 2. FTIR spectra of bare ZnO, CNDs/ZnO-0.1, CNDs/ZnO-0.3 and CNDs/ZnO-0.6 (**A**) and bare CNDs (**B**). XRD spectra of CNDs, ZnO, and CNDs/ZnO (**C**) and magnified view of XRD spectra for ZnO and CNDs/ZnO samples (**D**).

some differences were detected. These suggest that, while the functional groups were preserved during the synthesis, a structural rearrangement occurred leading to the formation of small dots.

The combination of CNDs with ZnO into hybrid mesocrystals, preserved the hexagonal structure of ZnO but, increasing the amount of CNDs during the doping, led in some alterations in the crystalline structure as revealed by a deeper XRD spectra analysis. Indeed, as shown in Fig. 2D, a shoulder appeared in the first three characteristic XRD peaks for CNDs/ZnO materials with higher CNDs content (i.e., CNDs/ZnO-0.3 and CNDs/ZnO-0.6). This feature suggests the presence of two distinct populations of crystallites with the same crystalline structure. Additionally, the peak corresponding to the (002) crystalline plane at $2\theta = 34^\circ$ became more pronounced with increasing CNDs content, thus indicating that the CNDs preferentially interact with ZnO through the (002) plane, leading to its expansion. This preferential interaction during synthesis was likely a critical factor influencing the structural transformations observed in the TEM images. The absence of the shoulder in the spectrum of CNDs/ZnO-0.1 (Fig. 2D) suggested that the relative amount of CNDs used in its preparation was insufficient to induce structural modification, making this sample like bare ZnO. As detailed in SI, the Scherrer equation was employed to determine the crystallite sizes of ZnO, CNDs/ZnO-0.1, CNDs/ZnO-0.3, and CNDs/ZnO-0.6, yielding values of 33.9 ± 4.8 nm, 30.5 ± 5.8 nm, 32.5 ± 10.2 nm, and 32.5 ± 5.6 nm, respectively. The optical properties of CNDs/ZnO mesocrystals were assessed to foresee the use in the photocatalytic tests. By UV-Diffuse Reflectance Spectroscopy (DRS), absorption properties of the samples were evaluated, and the bandgap values were estimated by applying Kubelka-Munk theory and constructing Tauc-plots.

As shown in Fig. 3A, CNDs/ZnO samples displayed an absorption band at $\lambda < 400$ nm, typical of ZnO which lacks absorption in the visible region [59]. However, CNDs/ZnO mesocrystals exerted an increasing absorption in the visible range becoming more pronounced at higher CNDs content. Indeed, as reported in Fig. 3, bare CNDs exhibited an absorption band across the entire range from 200 nm to 800 nm, like the behavior of HS precursor (Figure S5). This is because HS can absorb in the visible range due to charge interactions between electron donor and acceptor groups [60]. Since the functional groups of HS were retained during the synthesis, the resulting CNDs showed an absorption in the visible range similar to their precursor. Moreover, it is known that CNDs possess up-conversion properties that enable them to transform visible and near-infrared light into shorter wavelengths [61]. Specifically, CNDs/ZnO-0.1 sample exhibited a slight absorption in the visible range indicating that, even though the amount of CNDs was too low to significantly alter the ZnO crystalline structure, it was already sufficient to improve the optical properties. These findings, along with XRD analyses, confirm that the amount of CNDs used for ZnO doping, affected the final properties of the resulting hybrid materials. The bandgap energy values (Eg_s) were determined using Tauc plots (Fig. 3B). Notably, the CNDs/ZnO-0.1 had a E_g value (3.19 eV) slightly lower to that of bare ZnO (3.23 eV). On the other hand, a significant decrease in bandgap energy was detected for samples with a greater CND amount, such as CNDs/ZnO-0.3 and CNDs/ZnO-0.6, whose band gap energy value (3.04 eV) was significantly lower than that of bare ZnO.

3.2. Sunlight photodegradation of PHB microplastics mediated by CNDs/ZnO mesocrystals

The effects of sunlight-induced degradation of PHB MPs in the presence of CNDs/ZnO mesocrystals were monitored by ATR-FTIR analysis. As a reference, the FTIR spectrum of untreated PHB was first recorded (Figure S6A), which exhibited the characteristic peaks at 1719 cm^{-1}, 1268 cm^{-1}, 1122 cm^{-1}, and 1048 cm^{-1}, corresponding to C═O, C-O, and CO-O-CO stretching/vibrations [62]. ATR-FTIR analysis was then carried out after each photodegradation treatment, as shown in Figures S6B-S6F. In order to investigate the crystallinity degree of PHB, the band associated with C═O stretching was analyzed. This band is sensitive to the crystallization of PHB, with the 1720 cm^{-1} band arising from ordered crystalline C═O groups along with CH_3 groups, whereas the 1740 cm^{-1} band is associated with amorphous free C═O groups [63]. On this basis, the C═O band was deconvoluted using Gaussian curves ensuring that the sum of the areas of the peak is equal to 100. The deconvolution of the C═O band before and after the photodegradation treatment is shown in Fig. 4. It should be noted that the deconvolution of the peaks before and after photodegradation was achieved only by considering three or four components. The first two components were the 1740 cm^{-1} and 1720 cm^{-1} bands, which corresponded to the amorphous and crystalline phases, respectively. The other two components were located at approximately 1705 cm^{-1} and 1665 cm^{-1}. The 1705 cm^{-1} peak was associated with H-bonded C═O groups [64], likely due to water molecules adsorbed on the PHB films during photodegradation, acting as H-donors. Similarly, the 1665 cm^{-1} peak was associated with water molecules hydrogen-bonded to C═O groups [64].

The actual adsorption of water on PHB MPs has not been determined, hence the absolute crystallinity was not measured. For this reason, changes in the peak areas associated with water adsorption on PHB films were previously examined. As shown in Figure S7, the sum of these

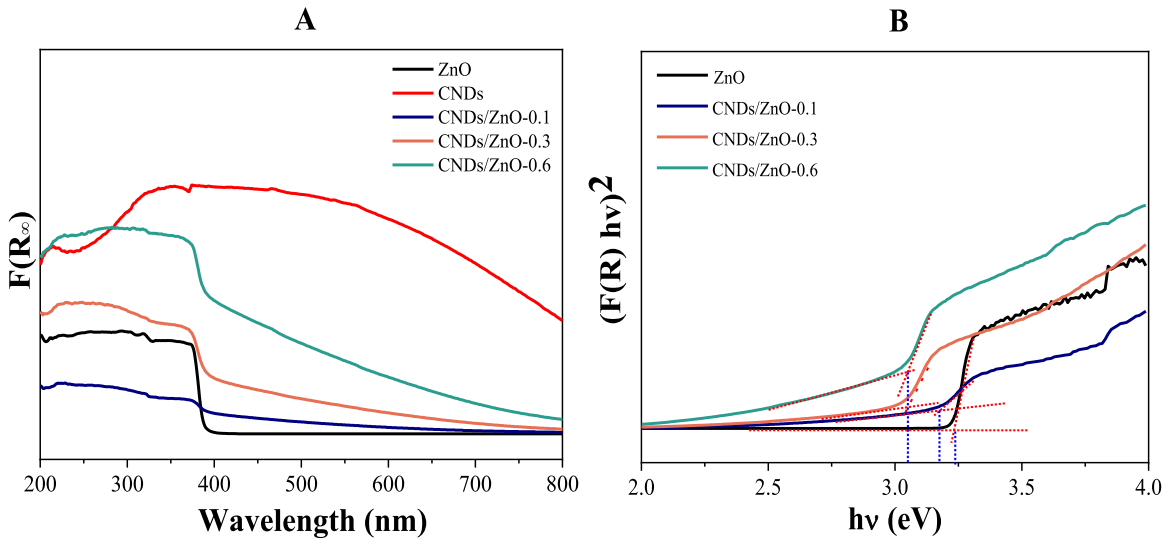

Fig. 3. UV-DRS absorption spectra (**A**), Tauc-plot spectra (**B**) of bare and hybrid samples.

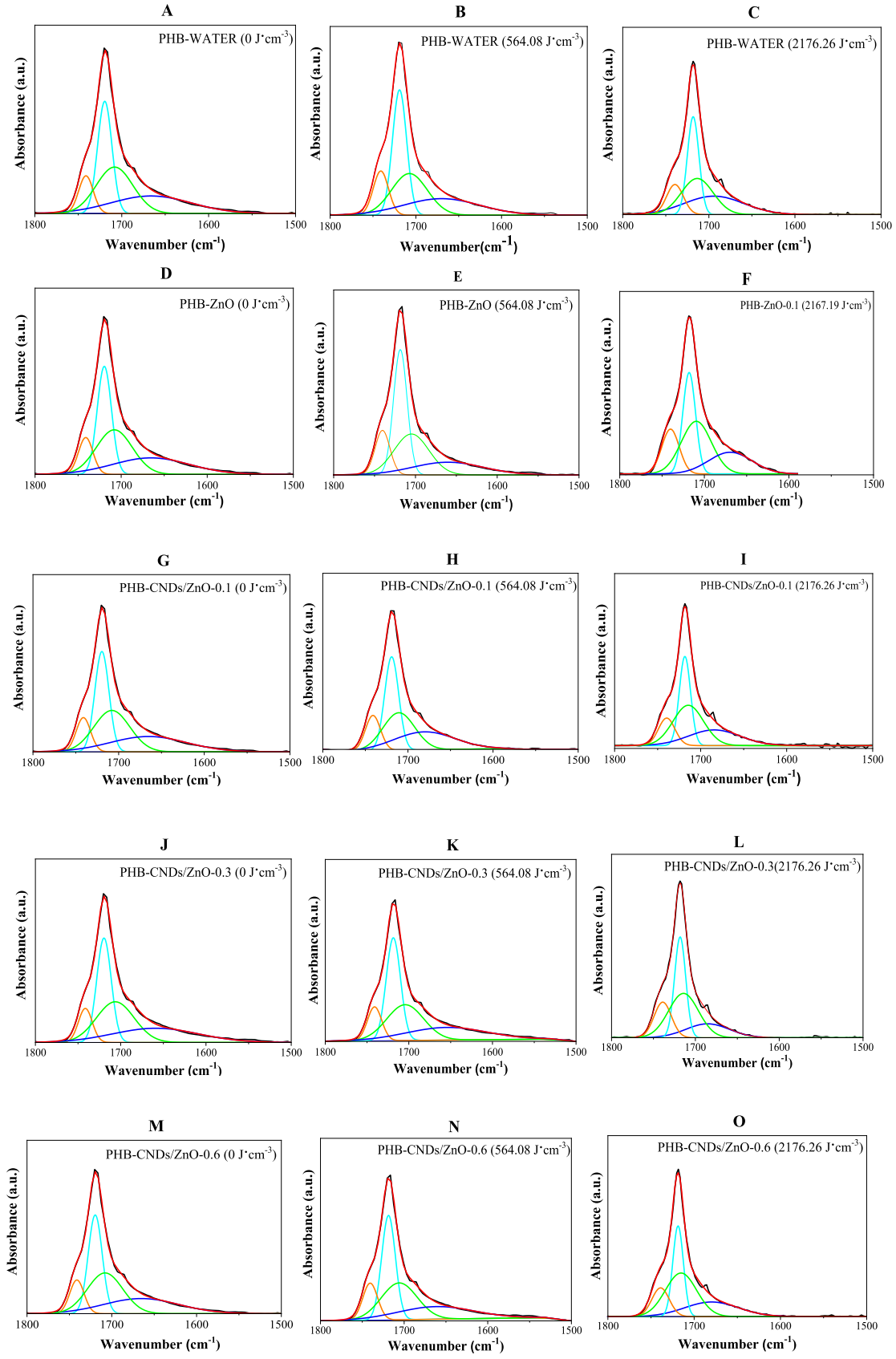

Fig. 4. Deconvolution of the carbonyl peak for PHB MPs treated with pure water at Q_{UV} of 0 J·cm^{-3} (A), 564.08 J·cm^{-3} (B) and 2176.26 J·cm^{-3} (C); treated with ZnO at Q_{UV} of 0 J·cm^{-3} (D), 564.08 J·cm^{-3} (E) and 2176 J·cm^{-3} (F); treated with CNDs/ZnO-0.1 at Q_{UV} of 0 J·cm^{-3} (G), 564.08 J·cm^{-3} (H), and 2176.26 J·cm^{-3} (I); treated with CNDs/ZnO-0.3 at Q_{UV} of 0 J·cm^{-3} (J), 564.08 J·cm^{-3} (K) and 2176.26 J·cm^{-3} (L); treated with CNDs/ZnO-0.6 at Q_{UV} of 0 J·cm^{-3} (M), 564.08 J·cm^{-3} (N) and 2176.26 J·cm^{-3} (O).

peaks remained nearly constant and, consequently, any scaling factor was applied when calculating the actual contributions of the crystalline and amorphous phases. Consequently, the ratios between the areas of the crystalline and amorphous phases calculated after each irradiation time interval were then normalized with respect to the untreated PHB. The trend of the area ratio for the crystalline peak (A_{1720}) and the amorphous one (A_{1740}) as a function Q_{UV} is reported in Fig. 5**A.** Here, a significant decrease in this ratio was observed across all samples during photo-treatments thus suggesting the progressive degradation of PHB MPs.

Specifically, it is noticeable that the samples treated with water alone exhibited the lowest photodegradation effect. This degradation likely resulted from thermal UVA radiation which caused changes in the molecular weight, chemical and crystalline structures, thermal and morphological properties, which are associated to the predominantly occurrence of macromolecule breakdown (e.g., chain scission via Norrish mechanisms), and to the crosslinking reactions occurring in the regions far from the surface with smaller oxygen availability and lower light penetration, as a consequence of the recombination of free radicals formed by the chain scission [65,66]. Conversely, the MPs samples treated in the presence of ZnO, CNDs/ZnO-0.3 and CNDs/ZnO-0.6 demonstrated more pronounced morphological modifications with similar patterns. The comparable behavior of ZnO and CNDs ZnO-0.1 could be attributed to the insufficient quantity of CNDs added to the system, which was too low to significantly modify the photoactivity of ZnO mesocrystals. This finding was further supported by XRD results showing that any crystalline modification occurred and by DRUV results which indicated no change in the bandgap for CNDs/ZnO-0.1 hybrid material. On the other hand, the lower structural variation observed in presence of CNDs/ZnO-0.6 than that exerted in presence of CNDs/ZnO-0.3 might be ascribed due to an excessively high concentration of CNDs, which covered the mesocrystals and hindered the proper interaction between solar radiation and ZnO particles (e.g., shielding effect), crucial for generating holes and electrons required for the photodegradation of PHB MPs. The carbonaceous component, which was rich in π-conjugated systems and intrinsic radicals typical of humic substances (and their derivatives), enhanced the charge separation and facilitated the electron transfer, thus reducing the electron–hole recombination produced upon excitation [67,68]. Also, the synergistic interaction between ZnO and CNDs promoted ROS generation, confirming that the mechanism occurs in a radical environment. The obtained results indicated that CNDs/ZnO-0.3 material showed the highest photocatalytic performance, thus suggesting that this CNDs concentration offered an optimal balance between surface coverage and photocatalytic activity. In order to further support this behavior, the crystallinity of PHB samples was evaluated by estimating the crystalline index, which represents the area of the peak of the crystalline phase relative to the total area of the XRD spectrum. The trends of the crystalline index determined from the XRD spectra of all samples (Figures S8) as referred to different Q_{UV} doses are shown Fig. 5B. These indicated that the crystallinity of PHB decreased by increasing the Q_{UV} dose but this effect was strongly influenced by the type of mesocrystals used as photocatalysts. In particular, the greater effect was induced by ZnO mesocrystals doped with low amounts of CNDs and, according to the evidence of FTIR analysis, CNDs/ZnO-0.3 sample exhibited the best performance if compared to bare ZnO or CNDs/ZnO-0.6, whose the high amount of CNDs hindered an efficient photodegradation activity.

3.3. Degradation in soil of PHB microplastics after CNDs/ZnO-mediated sunlight photo-treatment

In order to assess the effect of solar photocatalytic pre-treatment on the soil degradation process of PHB MPs, the degradation in soil burial of PHB not previously irradiated was compared with PHB samples previously exposed to sunlight irradiation for two different Q_{UV} dose, named as PHB- CNDs/ZnO-0.3 (564.08 J·cm^{-3}) and PHB-CNDs/ZnO-0.3 (2176.26 J·cm^{-3}), in the presence of CNDs/ZnO-0.3 which was the photoactive material previously identified as the more susceptible to photo-treatment if compared with those at lower (CNDs/ZnO-0.1) and higher (CNDs/ZnO-0.6) doping amounts of CNDs. Untreated and irradiated PHB-CNDs/ZnO-0.3 samples were buried in soil for 135 days, as described in Section 2.5. The weight loss of PHB samples during burial was reported in Fig. 6. Different degradation rates were observed for the investigated PHB MPs in soil. In detail, the weight of untreated PHB

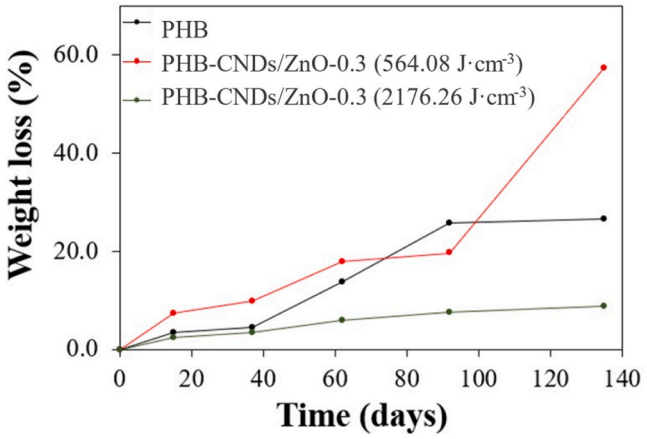

Fig. 6. Weight loss % of PHB MPs during soil burial.

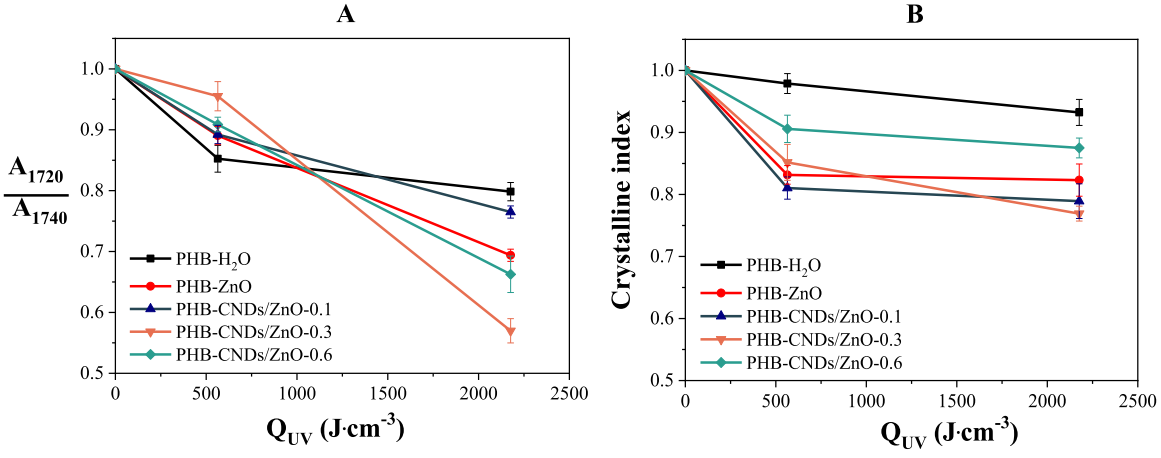

Fig. 5. Crystalline-to-amorphous ratio trend with Q_{UV} exposure (A) and crystalline index trend with Q_{UV} exposure (B).

remained almost unchanged with only a 3 % loss during the first 40 days. An increase in the weight loss percentage was recorded between 40 and 100 days of burial, reaching approximately 27 % after 135 days of soil burial. The initial incubation period of up to about 40 days aligns with previously reported literature data [23].

PHB-CNDs/ZnO-0.3 exposed to a Q_{UV} dose of 564.08 J·cm^{-3}, showed, the greatest weight loss during burial, at 135 days of burial, reaching a loss of about 57 %. Surprisingly, the PHB-CNDs/ZnO-0.3 (2176.26 J·cm^{-3}) sample presented the lowest weight loss (about 9 % after 135 days of burial), showing an initial incubation period of 40 days similar to the case of the untreated PHB. Gravimetric determination of the weight loss of PHB-CNDs/ZnO-0.3 samples during soil burial suggested a greater efficacy of the sunlight exposure to 564.08 J·cm^{-3}, whereas increasing the irradiation time of the treatment up to

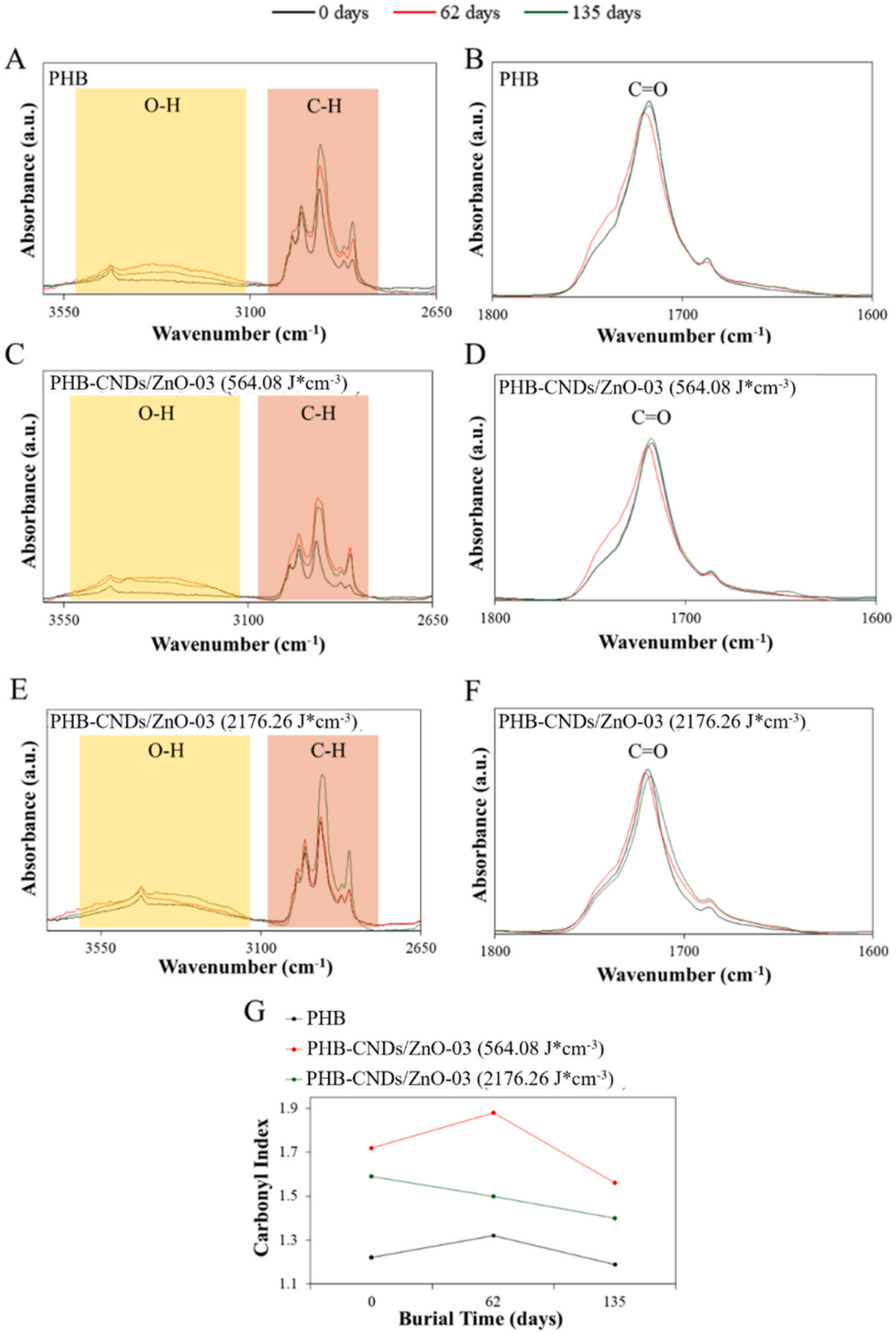

Fig. 7. FTIR spectra acquired during burial test and magnification of the carbonyl region respectively of PHB (A, B), PHB-CNDs/ZnO-0.3 (564.08 J·cm^{-3}) (C, D), PHB-CNDs/ZnO-0.3 (2176.26 J·cm^{-3}) (E, F). Trends of carbonyl index versus the burial time (G).

2176.26 J·cm^{-3} resulted in a slower degradation reaching weight loss lower than that of the untreated PHB.

The reduced degradability in soil of the samples exposed to sunlight for longer times could be due to an improved occurrence of the cross-linking reactions involving the free radicals (and/or ions) generated by the irradiation. These could favor a reorganization of the degraded molecules located underneath the most external layer, making the photo treated PHB MPs less biodegradable [65,66]. In order to better elucidate this unexpected trend, FTIR spectra of unexposed and sunlight exposed samples buried in soil were recorded, as reported in Fig. 7. All the spectra presented an increase in the absorption band in the range 3000–3500 cm^{-1}, related to the O-H stretching. For unexposed and sunlight exposed PHB samples, the band at 3437 cm^{-1} increased with burial time due to an increase in the OH groups as consequence of the formation of carboxylic acid and unsaturated groups, which represented a direct indication of PHB degradation during soil burial [65,69]. Furthermore, the PHB-CNDs/ZnO-0.3 (2176.26 J·cm^{-3}) sample exhibited a broadening and upshift of the band due to the hydroxyl stretching that could be attributed to the formation of hydrogen-bond among the carbonyl of the ester group of PHB and the hydroxyl groups formed during polymer hydrolysis [70]. In the C-H stretching region (2800–3200 cm^{-1}), six bands of semicrystalline PHB were identified: 3007 cm^{-1}, 2997 cm^{-1}, 2976 cm^{-1}, 2935 cm^{-1}, 2873 cm^{-1} and 2850 cm^{-1} [71]. A gradual increase in the intensity of these bands was observed with increasing burial time suggesting the development of PHB crystalline structure and the reorganization of crystal phase due to the degradation of material during burial. For PHB-CNDs/ZnO-0.3 (564.08 J·cm^{-3}), the presence of an absorption bands at 2927 cm^{-1} was detected. The bands at 2976 cm^{-1}, 2927 cm^{-1}, may be due to the crystal field splitting [71]. This phenomenon is reported to be caused by intermolecular or intramolecular interactions in the crystal unit or in the intramolecular interactions, related to the formation of the left-handed helix conformation of PHB, so that the occurrence of crystal field splitting PHB-CNDs/ZnO-0.3 (564.08 J·cm^{-3}) could indicate the occurrence of new intramolecular interactions as a consequence of degradation. Weak intramolecular interactions, such as hydrogen bonding C–H···O═C between two helical structures in PHB, were reported [72]. The absorption band at 1720 cm^{-1} was observed, which was due to C═O stretching vibration of PHB in the crystalline phase together with a broad band at 1740 cm^{-1} arising from the C═O stretching of amorphous PHB. The increase in the band at 1740 cm^{-1}, during burial, particularly in the case of PHB-CNDs/ZnO-0.3 (564.08 J·cm^{-3}), could suggest the formation of intermolecular hydrogen bonding between PHB chains in the amorphous phase [72]. The carbonyl index CI was calculated as the ratio between the intensity of the C═O bands at 1721 cm^{-1} and that of CH_3 group at 1278 cm^{-1} [73] and a decrease in CI values for both PHB-CNDs/ZnO-0.3 (564.08 J·cm^{-3}) and PHB-CNDs/ZnO-0.3 (2176.26 J·cm^{-3}) was observed after 135 days of burial [74], as shown in Fig. 7.

Burial strongly affected the surface morphologies of the samples as visible in Fig. 8. After 62 days of burial, samples presented strong surface erosion. The presence of spherulites on the film surface indicated that degradation was more effective on amorphous regions of PHB. It is known that enzyme responsible for hydrolysing PHB exerted a preference for chains in the amorphous phase during the early stages of soil degradation [65]. Several mechanisms were reported to explain the degradation of amorphous regions, such as the greater susceptibility to hydrolysis compared to crystalline regions [75,76] or of the easier degradation of the amorphous regions induced by bacteria [69]. After 135 days of aging the PHB-CNDs/ZnO-0.3 (564.08 J·cm^{-3}) sample appeared significantly more degraded than the other samples. This result was consistent with gravimetric analysis. Indeed, after 62 days of burial, the surface of PHB-CNDs/ZnO-0.3 (564.08 J·cm^{-3}) was homogeneously degraded, and after 135 days, the presence of spherulites was evident on the entire surface. These observations confirmed that the amorphous regions of the material degraded more rapidly, leaving the underlying spherulitic structures exposed [23]. However, it is worth noting that some studies have shown that certain semi-crystalline PHB - and, more generally, PHA - may degrade more efficiently due to favorable chain packing and enzyme-substrate interactions within crystalline

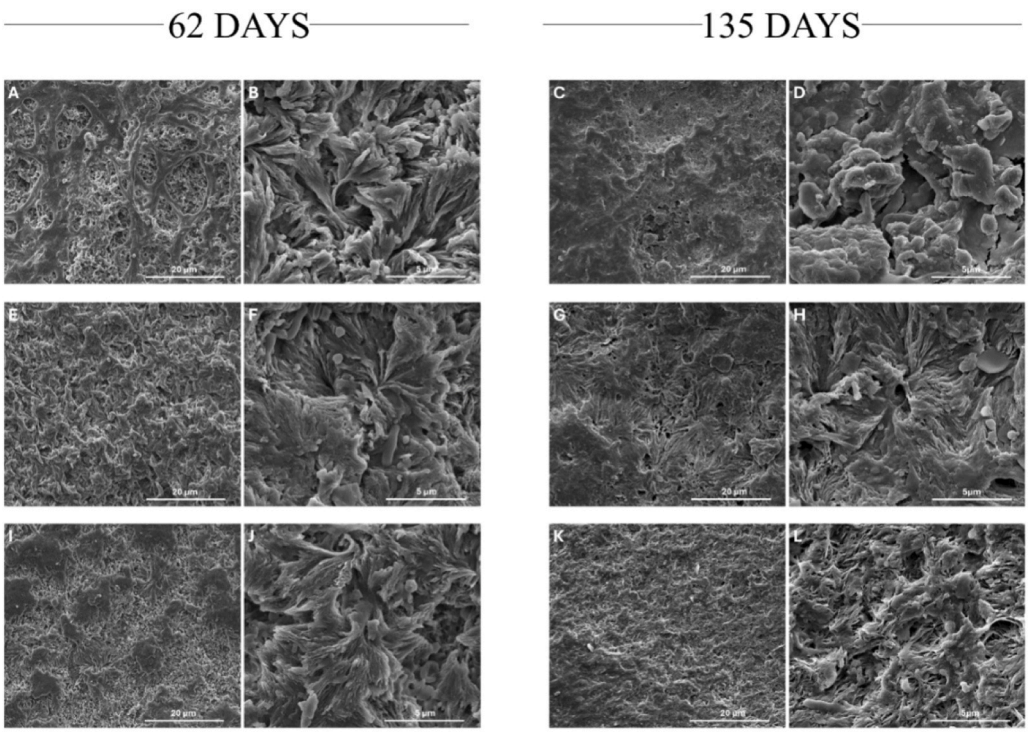

Fig. 8. SEM micrographs of unexposed and photo-exposed PHB MPs during burial test: PHB after 62 days (A, B) and 135 days (C, D) of degradation in soil; PHB-CNDs/ZnO-0.3 (564.08 J·cm^{-3}) after 62 days (E, F) and 135 days (G, H) of degradation in soil; PHB-CNDs/ZnO (2176.26 J·cm^{-3}) after 62 days (I, J) and 135 days (K, L) of degradation in soil.

domains [77,78]. For the PHB-CNDs/ZnO-03 (2176.26 J·cm^{-3}) samples, aged both at 62 days and 135 days of burial, the SEM observations on the surface of the samples were in agreement with the results collected by gravimetric analysis. Similarly to what observed for PHB MPs, degraded and non-degraded areas can be distinguished, indicating a non-homogeneous degradation process also in this case. In summary, the assessment would indicate that there are two opposite effects: the ratio crystalline/amorphous region and the degree of crosslinking. In particular, the photocatalytic process in presence of CNDs/ZnO-0.3 promoted the increase of the amorphous region of the polymeric matrix if compared with the PHB samples irradiated in absence of photocatalyst (CNDs/ZnO-0.x) or in presence of bare ZnO, but very prolonged irradiation times would generate an insufficient number of scissions in the polymer chain and, consequently, the produced fragments affected the structural re-organization of the inner chains (photo-induced cross-linking) thus disfavoring the degradation in soil. These results contributed to better elucidating the hypotheses reported by previous authors [66].

DSC thermograms, acquired during the first heating scan of the samples analyzed after burial test, are reported in Fig. 9. The thermal properties, such as melting and crystallization temperatures (T_m, T_c) and enthalpies (ΔH_m, ΔH_c) as well as crystallinity index (X_c), are summarized in Table S1. Unexposed PHB sample presented complex melting behavior during the first fusion event, with a main peak at 168 °C and a secondary peak at 183 °C. This behavior has been frequently reported in the literature for PHB and attributed to three main phenomena: simultaneous melting-recrystallization-remelting processes, presence of crystallites with different lamellar thickness, polymorphism [79]. The presence of the double melting peak for PHB MPs buried in soil was consistent with a possible reorganization of the crystals due to the degradation [80]. In fact, long well-ordered polymer chains crystallized more easily in thicker lamellae, while short and poorly ordered chains crystallized in lamellae with reduced thickness inducing the presence of multiple melting.

PHB-CNDs/ZnO-0.3 (564.08 J·cm^{-3}) and PHB-CNDs/ZnO-0.3 (2176.26 J·cm^{-3}) samples presented the main melting peak at 168 °C. During cooling scan, no differences were detected between PHB and PHB-CNDs/ZnO-0.3 (564.08 J·cm^{-3}) they presented a similar crystallization profile while PHB-CNDs/ZnO-0.3 (2176.26 J·cm^{-3}) presented a broadening of the crystallization peak with a slow shift of T_c to lower temperatures. X_c was strongly affected by the treatment performed with CNDs/ZnO. In fact, PHB-CNDs/ZnO (564.08 J·cm^{-3}) and PHB-CNDs/ZnO (2176.26 J·cm^{-3}) presented lower X_c value with respect to PHB after burial test ascribable to a reduction of the amorphous phase in PHB samples degraded during burial and to an increased degradation of PHB-CNDs/ZnO samples with modification of the crystalline phase.

3.4. Biofilm formation onto PHB microplastics after sunlight photo-treatment

A campaign based on submerged biofilm growth on the PHB MPs photo-treated alternatively in the presence of bare ZnO and hybrid CNDs/ZnO-0.3 mesocrystals with Q_{UV} of 2176.26 J·cm^{-3} was carried out to explore the effect of the photochemical treatment in boosting the microbial adhesion and biofilm formation. Biofilm 3D reconstructions of z-stack images, along with microscope images, were reported in Fig. 10A, while biovolume and substratum coverage were quantified with image analysis in Fig. 10B-C. Plastics contamination was separately analysed for each strain. Regarding the untreated samples, both strains couldn't colonize surfaces, exhibiting both no biovolume and substratum coverage. On the other hand, treatments improved surface ability to be colonised, more specifically ZnO treated samples were contaminated only by *B. subtilis*, while CNDs/ZnO-0.3 treated samples were heavily contaminated by both bacteria. These results aligned with the findings from photocatalytic and soil degradation studies. The higher biofilm growth on the MPs treated with CNDs/ZnO-0.3 could be attributed to a previous stronger photocatalytic degradation of the MPs that modified the surface of the MPs making it more sensible and vulnerable to microorganisms' adhesion [81]. Although the strains used were not specifically selected for their ability to degrade PHB, and therefore the observed biofilm could not be directly linked to enhanced biodegradation, the results clearly demonstrated that the photochemical treatment induced surface changes - both morphological and chemical - that promoted microbial colonization. Biofilm development is critical in the microbial degradation of polymers, as it increases residence time, local enzymatic activity, and the probability of interaction between microbes and the substrate [82,83]. In this context, the enhanced biofilm formation on pre-treated MPs may have reflected a higher microbial loading capacity, potentially influencing microbial transport dynamics in the environment. These findings suggested a direct relationship between the chemical, structural and morphological properties of MPs surface, opening to further investigations to clarify the mechanisms of interaction between microorganisms and MPs before and after the photoinduced treatments.

4. Conclusions

In the present investigation, the effect of photocatalytic induced degradation of PHB microplastics on their degradability in soil was investigated in order to better clarify the beneficial effect of solar light-driven strategy. To this aim, ZnO mesocrystals doped with bioderived carbon nanodots at different amounts were designed and prepared to be used as photocatalysts for the degradation of PHB MPs under sunlight.

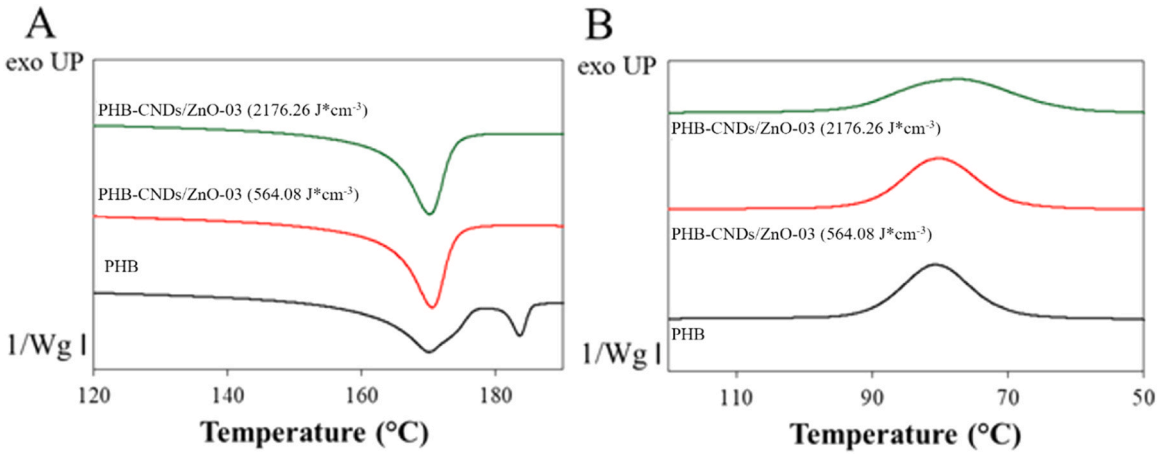

Fig. 9. DSC thermograms of untreated and photo-treated PHB MPs after aging in soil during the first heating scan (**A**) and during cooling run (**B**).

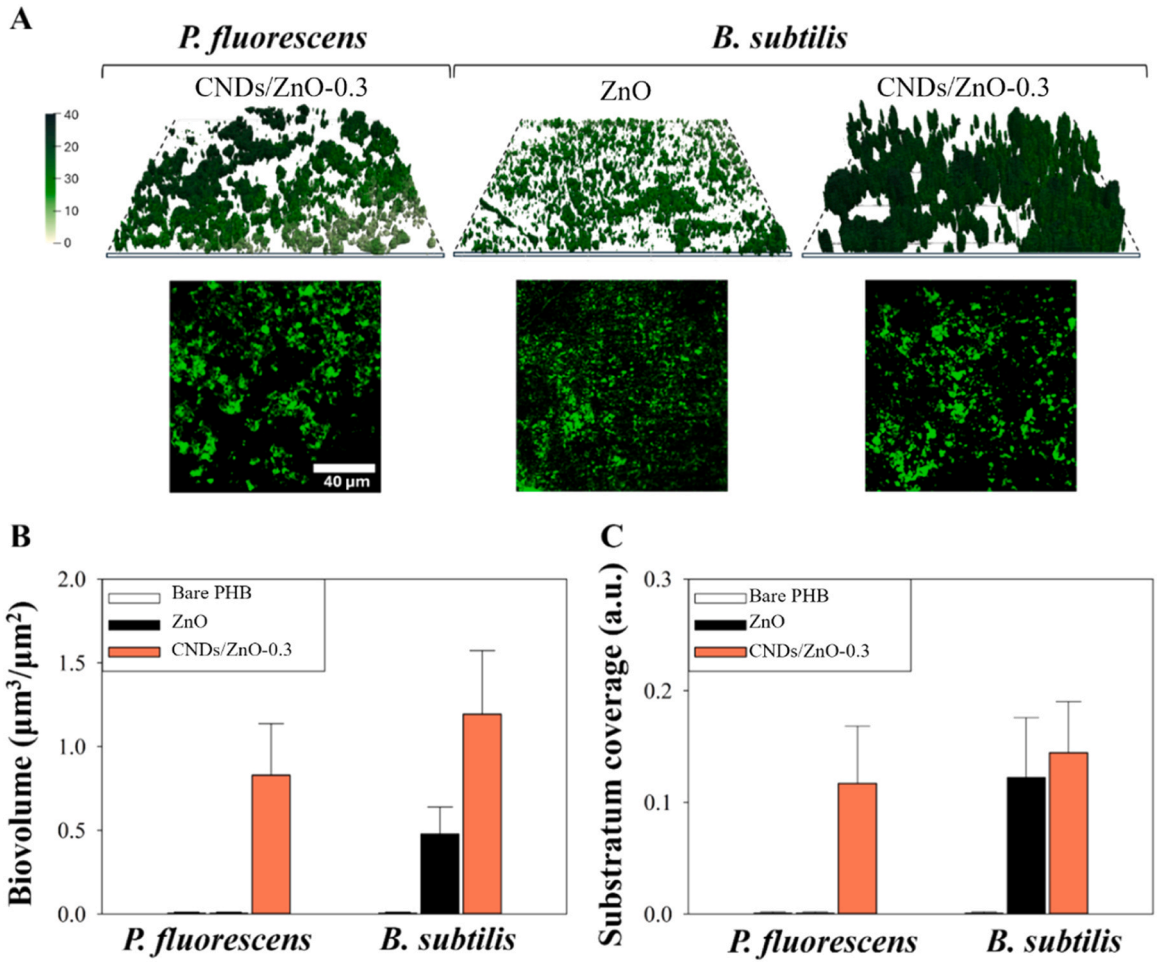

Fig. 10. Biofilm growth on differently treated microplastic coupons. 3D reconstructions obtained in Paraview from z-stack CLSM images, depicted below, of the P. fluorescens SBW25 and B. subtilis NDmed biofilms grown on microplastic coupons with different treatments: ZnO and CNDs/ZnO-0.3. P. fluorescens biofilm images on ZnO-treated and bare MPs and B. subtilis biofilm images on bare MPs were omitted due to lack of surface colonization. Colorimetric scale bar depicting biofilm thickness in µm was reported on the left (A). Biofilm volume of P. fluorescens and B. subtilis, normalized to the observed surface area for each type of MPs samples (B). Substratum coverage of P. fluorescens and B. subtilis biofilms for each type of MPs samples (C).

First of all, the hybrid CNDs/ZnO-0.3 material showed the highest photocatalytic activity with respect to bare ZnO and CNDs/ZnO mesocrystals doped at different ratios, thus indicating that an adequate amount of carbon nanodots can reduced the electron-hole recombination rate without light shielding for an excessive ZnO surface covering by carbon nanodots. Moreover. weight loss analysis, SEM, and DSC/TGA results revealed that PHB MPs photo irradiated in presence CNDs/ZnO-0.3 at a Q_{UV} of 564 J·cm^{-3} exhibited significantly higher degradation in soil than untreated samples due to a marked increase of the amorphous region of the polymeric matrix. However, PHB samples exposed to solar light for higher irradiation times (Q_{UV} of 2167 J·cm^{-3}) showed a reduced degradation in soil thus indicating that excessively prolonged photocatalytic treatment negatively impacted soil degradation efficiency as the possible consequence of a structural reorganization of the reacting polymeric chain molecules through crosslinking radical process which reduced the PHB MPs biodegradability. The preliminary study on the biofilm growth indicated that photodegraded PHB MPs treated with CNDs/ZnO-0.3 exhibited enhanced bacterial colonization, thus proposing a direct correlation between surface modifications and degradation in soil. These results highlighted a critical balance in the photodegradation strategies, while light-activated modification can support soil degradation, an excessive exposure may hinder it. This insight should be essential for the further design of biodegradable plastics embedded with photocatalytic additives, enabling light-responsive degradation tuned to real-world environmental conditions. Definitely, the obtained findings highlighted the key role of the dosage of CNDs to efficiently dope ZnO mesocrystals as well as the irradiation time/yield in order to induce the decisive chemical, structural and morphological changes of MPs for enhancing degradability and microbial colonization. These findings helped define key criteria for developing an integrated strategy that combined abiotic and biotic degradation mechanisms to mitigate the accumulation of PHB-based microplastics in the environment. Although the photocatalytic tests were performed in simplified aqueous systems and the direct use of dispersed photocatalysts in natural environments was not easily feasible, this study provided a proof-of-concept for integrating photocatalysis and biodegradation into more scalable and environmentally safe material designs. Future research should further investigate the photochemical mechanisms involved in prolonged irradiation and broaden the study of microbial colonization under diverse environmental conditions to guide the design of next-generation self-degrading bioplastics.

Environmental implications

The study highlights a promising environmentally adaptive strategy to mitigate microplastic pollution by integrating photocatalytic pretreatment with natural biodegradation. The use of biowaste-derived carbon-doped ZnO mesocrystals accelerates the degradation of polyhydroxybutyrate microplastics under sunlight, enhancing microbial colonization and biofilm formation. By tailoring irradiation time and

photocatalyst composition, this approach modifies microplastic surface properties to boost biodegradability while avoiding excessive photodegradation that may hinder microbial breakdown. These findings support the design of next-generation biodegradable plastics with tuneable degradation profiles, aligning with natural environmental processes and contributing to a more effective, sustainable reduction of plastic pollution.

CRediT authorship contribution statement

Mariacristina Cocca: Writing – review & editing, Visualization, Validation, Methodology, Investigation, Data curation. **Beate Förster:** Investigation, Formal analysis, Data curation. **Gennaro Gentile:** Investigation, Formal analysis, Data curation. **Raffaele Marotta:** Writing – review & editing, Visualization, Validation, Methodology, Conceptualization. **Sergio Caserta:** Writing – review & editing, Visualization, Methodology, Data curation. **Immacolata Liotta:** Writing – original draft, Investigation, Formal analysis, Data curation. **Marica Muscetta:** Writing – review & editing, Writing – original draft, Supervision, Methodology, Formal analysis, Conceptualization. **Daniele Marra:** Investigation, Formal analysis, Data curation. **Moreno Rizzo:** Investigation, Formal analysis. **Simone Russo:** Writing – review & editing, Writing – original draft, Methodology, Investigation, Formal analysis, Conceptualization. **Giuseppe Vitiello:** Writing – review & editing, Validation, Supervision, Project administration, Methodology, Funding acquisition, Conceptualization.

Declaration of Competing Interest

The authors declare that they have no known competing financial interests or personal relationships that could have appeared to influence the work reported in this paper.

Acknowledgements

The authors thank Verde Vita S.r.l company for providing the agri-food compost.

The preparation of PHB microplastics, their degradation in soil was financial supported by the Project - Biomonitoraggio di micro e nanoplastiche biodegradabili: dall'ambiente all'uomo in una prospettiva one health (BioPlast4Safe) - with the technical and economic support of the Italian Ministry of Health – PNC. The authors thanks Mrs. Maria Cristina Del Barone of LAMeST laboratory of the Institute for Polymers, Composites and Biomaterials, who is gratefully acknowledged for her technical support in SEM analyses of PHB MPs.

Biofilm growth and analysis work was financial supported by ESA (research projects OSIP IDEA: I-2021–03382), PRIN 2022 PNRR P20225AEF4 project and Space It Up project funded by the Italian Space Agency, ASI, and the Ministry of University and Research, MUR, under contract n. 2024–5-E.0 - CUP n. I53D24000060005. Dr. Romain Briandet is gratefully acknowledged for providing the *P. fluorescens* SBW25 and *B. subtilis* NDmed bacterial strains. Prof. Stefano Guido is gratefully acknowledged for helpful discussions and suggestions.

Appendix A. Supporting information

Supplementary data associated with this article can be found in the online version at doi:10.1016/j.jhazmat.2025.139933.

Data availability

Data will be made available on request.

References

[1] Ilyas, M., Ahmad, W., Khan, H., Yousaf, S., Khan, K., Nazir, S., 2018. Plastic waste as a significant threat to environment – a systematic literature review. Rev Environ Health 33, 383–406. https://doi.org/10.1515/reveh-2017-0035.
[2] Nayanathara Thathsarani Pilapitiya, P.G.C., Ratnayake, A.S., 2024. The world of plastic waste: a review. Clean Mater 11, 100220. https://doi.org/10.1016/j.clema.2024.100220.
[3] Pan, D., Su, F., Liu, C., Guo, Z., 2020. Research progress for plastic waste management and manufacture of value-added products. Adv Compos Hybrid Mater 3, 443–461. https://doi.org/10.1007/s42114-020-00190-0.
[4] Jahangiri, F., Mohanty, A.K., Pal, A.K., Shankar, S., Rodriguez-Uribe, A., Clemmer, R., et al., 2024. PHBV coating on biodegradable plastic sheet: effect of coating on morphological, mechanical and barrier properties. Prog Org Coat 189, 108270. https://doi.org/10.1016/j.porgcoat.2024.108270.
[5] Gupta, R.K., Agarwal, S., Mukhopadhyay, P., 2024. Plastics in buildings and construction. Applied Plastics Engineering Handbook. Elsevier, pp. 683–703.
[6] Lamontagne, N.D., 2019. Polymers help boost performance of Next-Generation electronics. Plast Eng 75, 30–33. https://doi.org/10.1002/peng.20091.
[7] Zhou, C., Bi, R., Su, C., Liu, W., Wang, T., 2022. The emerging issue of microplastics in marine environment: a bibliometric analysis from 2004 to 2020. Mar Pollut Bull 179, 113712. https://doi.org/10.1016/j.marpolbul.2022.113712.
[8] Focardi, A., Moore, L.R., Raina, J.-B., Seymour, J.R., Paulsen, I.T., Tetu, S.G., 2022. Plastic leachates impair picophytoplankton and dramatically reshape the marine microbiome. Microbiome 10, 179. https://doi.org/10.1186/s40168-022-01369-x.
[9] Ahmed, R., Hamid, A.K., Krebsbach, S.A., He, J., Wang, D., 2022. Critical review of microplastics removal from the environment. Chemosphere 293, 133557. https://doi.org/10.1016/j.chemosphere.2022.133557.
[10] Padervand, M., Lichtfouse, E., Robert, D., Wang, C., 2020. Removal of microplastics from the environment. A review. Environ Chem Lett 18, 807–828. https://doi.org/10.1007/s10311-020-00983-1.
[11] Lambert, S., Scherer, C., Wagner, M., 2017. Ecotoxicity testing of microplastics: considering the heterogeneity of physicochemical properties. Integr Environ Assess Manag 13, 470–475. https://doi.org/10.1002/ieam.1901.
[12] Strungaru, S.-A., Jijie, R., Nicoara, M., Plavan, G., Faggio, C., 2019. Micro- (nano) plastics in freshwater ecosystems: abundance, toxicological impact and quantification methodology. TrAC Trends Anal Chem 110, 116–128. https://doi.org/10.1016/j.trac.2018.10.025.
[13] Cverenkárová, K., Valachovičová, M., Mackuľak, T., Žemlička, L., Bírošová, L., 2021. Microplastics in the food chain. Life 11, 1349. https://doi.org/10.3390/life11121349.
[14] Santonicola, S., Volgare, M., Cocca, M., Dorigato, G., Giaccone, V., Colavita, G., 2023. Impact of fibrous microplastic pollution on commercial seafood and consumer health: a review. Animals 13, 1736. https://doi.org/10.3390/ani13111736.
[15] Winiarska, E., Jutel, M., Zemelka-Wiacek, M., 2024. The potential impact of nano- and microplastics on human health: understanding human health risks. Environ Res 251, 118535. https://doi.org/10.1016/j.envres.2024.118535.
[16] Sharma, S., Basu, S., Shetti, N.P., Nadagouda, M.N., Aminabhavi, T.M., 2021. Microplastics in the environment: occurrence, perils, and eradication. Chem Eng J 408, 127317. https://doi.org/10.1016/j.cej.2020.127317.
[17] Rasheed, A., Sharma, N., Surampalli, R.Y., Das, S., 2023. Evaluating treatment solutions: critical review on technologies employed for microplastic removal from water matrices. Curr Opin Environ Sci Health 36, 100516. https://doi.org/10.1016/j.coesh.2023.100516.
[18] Manfra, L., Marengo, V., Libralato, G., Costantini, M., De Falco, F., Cocca, M., 2021. Biodegradable polymers: a real opportunity to solve marine plastic pollution? J Hazard Mater 416, 125763. https://doi.org/10.1016/j.jhazmat.2021.125763.
[19] Tokiwa, Y., Calabia, B.P., 2007. Biodegradability and biodegradation of polyesters. J Polym Environ 15, 259–267. https://doi.org/10.1007/s10924-007-0066-3.
[20] Wei, X.-F., Bao, R.-Y., Cao, Z.-Q., Yang, W., Xie, B.-H., Yang, M.-B., 2014. Stereocomplex crystallite network in asymmetric PLLA/PDLA blends: formation, structure, and confining effect on the crystallization rate of homocrystallites. Macromolecules 47, 1439–1448. https://doi.org/10.1021/ma402653a.
[21] Wei, X.-F., Capezza, A.J., Cui, Y., Li, L., Hakonen, A., Liu, B., et al., 2022. Millions of microplastics released from a biodegradable polymer during biodegradation/enzymatic hydrolysis. Water Res 211, 118068. https://doi.org/10.1016/j.watres.2022.118068.
[22] McAdam, B., Brennan Fournet, M., McDonald, P., Mojicevic, M., 2020. Production of polyhydroxybutyrate (PHB) and factors impacting its chemical and mechanical characteristics. Polymers 12, 2908. https://doi.org/10.3390/polym12122908.
[23] De Falco, F., Avolio, R., Errico, M.E., Di Pace, E., Avella, M., Cocca, M., et al., 2021. Comparison of biodegradable polyesters degradation behavior in sand. J Hazard Mater 416, 126231. https://doi.org/10.1016/j.jhazmat.2021.126231.
[24] González-Pleiter, M., Tamayo-Belda, M., Pulido-Reyes, G., Amariei, G., Leganés, F., Rosal, R., et al., 2019. Secondary nanoplastics released from a biodegradable microplastic severely impact freshwater environments. Environ Sci Nano 6, 1382–1392. https://doi.org/10.1039/C8EN01427B.
[25] Viel, T., Cocca, M., Manfra, L., Caramiello, D., Libralato, G., Zupo, V., et al., 2023. Effects of biodegradable-based microplastics in paracentrotus lividus lmk embryos: morphological and gene expression analysis. Environ Pollut 334, 122129. https://doi.org/10.1016/j.envpol.2023.122129.
[26] Lv, H., Park, J., Lim, H.K., Abraham, I.J., Yin, X., Gao, Y., et al., 2024. Impacts of polyhydroxybutyrate (PHB) microplastic exposure on physiology and metabolic

profiles of litopenaeus vannamei. Sci Total Environ 951, 175588. https://doi.org/10.1016/j.scitotenv.2024.175588.
[27] Ciuffi, B., Fratini, E., Rosi, L., 2024. Plastic pretreatment: the key for efficient enzymatic and biodegradation processes. Polym Degrad Stab 222, 110698. https://doi.org/10.1016/j.polymdegradstab.2024.110698.
[28] Bule Možar, K., Milološa, M., Martinjak, V., Cvetnić, M., Kušić, H., Bolanča, T., et al., 2023. Potential of advanced oxidation as pretreatment for microplastics biodegradation. Separations 10, 132. https://doi.org/10.3390/separations10020132.
[29] Ateia, M., Alalm, M.G., Awfa, D., Johnson, M.S., Yoshimura, C., 2020. Modeling the degradation and disinfection of water pollutants by photocatalysts and composites: a critical review. Sci Total Environ 698, 134197. https://doi.org/10.1016/j.scitotenv.2019.134197.
[30] Ge, J., Zhang, Z., Ouyang, Z., Shang, M., Liu, P., Li, H., et al., 2022. Photocatalytic degradation of (micro)plastics using TiO2-based and other catalysts: properties, influencing factor, and mechanism. Environ Res 209, 112729. https://doi.org/10.1016/j.envres.2022.112729.
[31] Surana, M., Pattanayak, D.S., Yadav, V., Singh, V.K., Pal, D., 2024. An insight decipher on photocatalytic degradation of microplastics: mechanism, limitations, and future outlook. Environ Res 247, 118268. https://doi.org/10.1016/j.envres.2024.118268.
[32] Krishnan, A., Swarnalal, A., Das, D., Krishnan, M., Saji, V.S., Shibli, S.M.A., 2024. A review on transition metal oxides based photocatalysts for degradation of synthetic organic pollutants. J Environ Sci 139, 389–417. https://doi.org/10.1016/j.jes.2023.02.051.
[33] Pascariu, P., Gherasim, C., Airinei, A., 2023. Metal oxide nanostructures (MONs) as photocatalysts for ciprofloxacin degradation. Int J Mol Sci 24, 9564. https://doi.org/10.3390/ijms24119564.
[34] He, Y., Rehman, A.U., Xu, M., Not, C.A., Ng, A.M.C., Djurišić, A.B., 2023. Photocatalytic degradation of different types of microplastics by TiOx/ZnO tetrapod photocatalysts. Heliyon 9, e22562. https://doi.org/10.1016/j.heliyon.2023.e22562.
[35] Singh, K., Nancy, Bhattu, M., Singh, G., Mubarak, N.M., Singh, J., 2023. Light-absorption-driven photocatalysis and antimicrobial potential of PVP-capped zinc oxide nanoparticles. Sci Rep 13, 13886. https://doi.org/10.1038/s41598-023-41103-7.
[36] Goel, S., Sinha, N., Yadav, H., Joseph, A.J., Kumar, B., 2017. Experimental investigation on the structural, dielectric, ferroelectric and piezoelectric properties of la doped ZnO nanoparticles and their application in dye-sensitized solar cells. Phys E Low Dimens Syst Nanostruct 91, 72–81. https://doi.org/10.1016/j.physe.2017.04.010.
[37] Sunitha, A.P., Sandeep, K., Praveen, P., Saji, K.J., 2020. Upconverting carbon quantum dots: an eco-friendly material for light energy harvesting and bio-imaging. Mater Today Proc 33, 1298–1300. https://doi.org/10.1016/j.matpr.2020.03.822.
[38] Wang, X., Cao, L., Lu, F., Meziani, M.J., Li, H., Qi, G., et al., 2009. Photoinduced electron transfers with carbon dots. Chem Commun 3774. https://doi.org/10.1039/b906252a.
[39] Xu, J.-J., Lu, Y.-N., Tao, F.-F., Liang, P.-F., Zhang, P.-A., 2023. ZnO nanoparticles modified by carbon quantum dots for the photocatalytic removal of synthetic pigment pollutants. ACS Omega 8, 7845–7857. https://doi.org/10.1021/acsomega.2c07591.
[40] Vitiello, G., Iervolino, G., Imparato, C., Rea, I., Borbone, F., De Stefano, L., et al., 2021. F-doped ZnO nano- and meso-crystals with enhanced photocatalytic activity in diclofenac degradation. Sci Total Environ 762, 143066. https://doi.org/10.1016/j.scitotenv.2020.143066.
[41] Spasiano, D., Marotta, R., Malato, S., Fernandez-Ibañez, P., Di Somma, I., 2015. Solar photocatalysis: materials, reactors, some commercial, and pre-industrialized applications. A comprehensive approach. Appl Catal B 170–171, 90–123. https://doi.org/10.1016/j.apcatb.2014.12.050.
[42] Podstawczyńska A., 2009. UV and global solar radiation in Łódź, Central Poland. International Journal of Climatology n/a-n/a. https://doi.org/10.1002/joc.1864.
[43] Russo, S., Muscetta, M., Amato, P., Venezia, V., Verrillo, M., Rega, R., et al., 2024. Humic substance/metal-oxide multifunctional nanoparticles as advanced antibacterial-antimycotic agents and photocatalysts for the degradation of PLA microplastics under UVA/solar radiation. Chemosphere 346, 140605. https://doi.org/10.1016/j.chemosphere.2023.140605.
[44] Thellen, C., Coyne, M., Froio, D., Auerbach, M., Wirsen, C., Ratto, J.A., 2008. A processing, characterization and marine biodegradation study of Melt-Extruded polyhydroxyalkanoate (PHA) films. J Polym Environ 16, 1–11. https://doi.org/10.1007/s10924-008-0079-6.
[45] Dergham, Y., Le Coq, D., Bridier, A., Sanchez-Vizuete, P., Jbara, H., Deschamps, J., et al., 2023. Bacillus subtilis NDmed, a model strain for biofilm genetic studies. Biofilm 6, 100152. https://doi.org/10.1016/j.bioflm.2023.100152.
[46] Marra, D., Orillo, E., Toscano, G., Petala, M., Karapantsios, T.D., Caserta, S., 2024. The role of air relative humidity on the wettability of pseudomonas fluorescens AR11 biofilms. Colloids Surf B Biointerfaces 237, 113831. https://doi.org/10.1016/j.colsurfb.2024.113831.
[47] Hartmann, R., Jeckel, H., Jelli, E., Singh, P.K., Vaidya, S., Bayer, M., et al., 2021. Quantitative image analysis of microbial communities with BiofilmQ. Nat Microbiol 6, 151–156. https://doi.org/10.1038/s41564-020-00817-4.
[48] Thongam, D.D., Gupta, J., Sahu, N.K., 2019. Effect of induced defects on the properties of ZnO nanocrystals: surfactant role and spectroscopic analysis. SN Appl Sci 1, 1030. https://doi.org/10.1007/s42452-019-1058-3.
[49] Nandiyanto, A.B.D., Oktiani, R., Ragadhita, R., 2019. How to read and interpret FTIR spectroscope of organic material. Indones J Sci Technol 4, 97. https://doi.org/10.17509/ijost.v4i1.15806.
[50] Prasannan, A., Imae, T., 2013. One-Pot synthesis of fluorescent carbon dots from Orange waste peels. Ind Eng Chem Res 52, 15673–15678. https://doi.org/10.1021/ie402421s.
[51] Himaja, A.L., Karthik, P.S., Sreedhar, B., Singh, S.P., 2014. Synthesis of carbon dots from kitchen waste: conversion of waste to value added product. J Fluor 24, 1767–1773. https://doi.org/10.1007/s10895-014-1465-1.
[52] Xiong, G., Pal, U., Serrano, J.G., Ucer, K.B., Williams, R.T., 2006. Photoluminesence and FTIR study of ZnO nanoparticles: the impurity and defect perspective. Phys Status Solidi C 3, 3577–3581. https://doi.org/10.1002/pssc.200672164.
[53] Kang, X., Chatzitakis, A., Aarholt, T., Sun, X., Negri, C., Norby, T., 2022. Facet-engineered TiO $_2$ nanomaterials reveal the role of water–oxide interactions in surface protonic conduction. J Mater Chem A Mater 10, 218–227. https://doi.org/10.1039/D1TA06075A.
[54] Boruah, A., Saikia, M., Das, T., Goswamee, R.L., Saikia, B.K., 2020. Blue-emitting fluorescent carbon quantum dots from waste biomass sources and their application in fluoride ion detection in water. J Photochem Photobio B 209, 111940. https://doi.org/10.1016/j.jphotobiol.2020.111940.
[55] Antony Lilly Grace, M., Veerabhadra Rao, K., Anuradha, K., Judith Jayarani, A., Arun kumar, A., Rathika, A., 2023. X-ray analysis and size-strain plot of zinc oxide nanoparticles by Williamson-Hall. Mater Today Proc 92, 1334–1339. https://doi.org/10.1016/j.matpr.2023.05.492.
[56] Benali, H., Hartiti, B., Lmai, F., Batan, A., Fadili, S., Thevenin, P., 2024. Synthesis and characterization of Al-doped ZnO thin-films for photovoltaic applications. Mater Today Proc. https://doi.org/10.1016/j.matpr.2024.06.012.
[57] Arul, V., Chandrasekaran, P., Sivaraman, G., Sethuraman, M.G., 2023. Biogenic preparation of undoped and heteroatoms doped carbon dots: effect of heteroatoms doping in fluorescence, catalytic ability and multicolour in-vitro bio-imaging applications - a comparative study. Mater Res Bull 162, 112204. https://doi.org/10.1016/j.materresbull.2023.112204.
[58] Ding, Z., Shen, C., Han, J., Zheng, G., Ni, Q., Song, R., et al., 2023. In situ confining citric Acid-Derived carbon dots for Full-Color Room-Temperature phosphorescence. Small 19. https://doi.org/10.1002/smll.202205916.
[59] Moussawi, R.N., Patra, D., 2016. Modification of nanostructured ZnO surfaces with curcumin: fluorescence-based sensing for arsenic and improving arsenic removal by ZnO. RSC Adv 6, 17256–17268. https://doi.org/10.1039/C5RA20221C.
[60] Del Vecchio, R., Blough, N.V., 2004. On the origin of the optical properties of humic substances. Environ Sci Technol 38, 3885–3891. https://doi.org/10.1021/es049912h.
[61] Gao, D., Zhao, P., Lyu, B., Li, Y., Hou, Y., Ma, J., 2020. Carbon quantum dots decorated on ZnO nanoparticles: an efficient visible-light responsive antibacterial agents. Appl Organomet Chem 34. https://doi.org/10.1002/aoc.5665.
[62] Sakaguti, K., Wang, S., 2021. Preparation of Poly(3-hydroxybutyrate-b-ε-caprolactone) by reactive extrusion and production of electrospun fibrous mats. J Braz Chem Soc. https://doi.org/10.21577/0103-5053.20200186.
[63] Padermshoke, A., Katsumoto, Y., Sato, H., Ekgasit, S., Noda, I., Ozaki, Y., 2005. Melting behavior of poly(3-hydroxybutyrate) investigated by two-dimensional infrared correlation spectroscopy. Spectrochim Acta A Mol Biomol Spectrosc 61, 541–550. https://doi.org/10.1016/j.saa.2004.05.004.
[64] Yoshie, N., Oike, Y., Kasuya, K., Doi, Y., Inoue, Y., 2002. Change of surface structure of Poly(3-hydroxybutyrate) film upon enzymatic hydrolysis by PHB depolymerase. Biomacromolecules 3, 1320–1326. https://doi.org/10.1021/bm020077a.
[65] Sadi, R.K., Fechine, G.J.M., Demarquette, N.R., 2010. Photodegradation of poly(3-hydroxybutyrate). Polym Degrad Stab 95, 2318–2327. https://doi.org/10.1016/j.polymdegradstab.2010.09.003.
[66] Lim, J., Kim, J., 2016. UV-photodegradation of poly(3-hydroxybutyrate-co-3-hydroxyhexanoate) (PHB-HHx). Macromol Res 24, 9–13. https://doi.org/10.1007/s13233-016-4004-x.
[67] Amato, P., Muscetta, M., Venezia, V., Cocca, M., Gentile, G., Castaldo, R., et al., 2023. Eco-sustainable design of humic acids-doped ZnO nanoparticles for UVA/light photocatalytic degradation of LLDPE and PLA plastics. J Environ Chem Eng 11, 109003. https://doi.org/10.1016/j.jece.2022.109003.
[68] Venezia, V., Verrillo, M., Gallucci, N., Di Girolamo, R., Luciani, G., D'Errico, G., et al., 2023. Exploiting bioderived humic acids: a molecular combination with ZnO nanoparticles leads to nanostructured hybrid interfaces with enhanced pro-oxidant and antibacterial activity. J Environ Chem Eng 11, 108973. https://doi.org/10.1016/j.jece.2022.108973.
[69] Julinová, M., Šašinková, D., Minařík, A., Kaszonyiová, M., Kalendová, A., Kadlečková, M., et al., 2023. Comprehensive biodegradation analysis of chemically modified Poly(3-hydroxybutyrate) materials with different crystal structures. Biomacromolecules 24, 4939–4957. https://doi.org/10.1021/acs.biomac.3c00623.
[70] Díez-Pascual, A., Díez-Vicente, A., 2014. Poly(3-hydroxybutyrate)/ZnO bionanocomposites with improved mechanical, barrier and antibacterial properties. Int J Mol Sci 15, 10950–10973. https://doi.org/10.3390/ijms150610950.
[71] Zhang, J., Sato, H., Noda, I., Ozaki, Y., 2005. Conformation rearrangement and molecular dynamics of Poly(3-hydroxybutyrate) during the Melt-Crystallization process investigated by infrared and Two-Dimensional infrared correlation spectroscopy. Macromolecules 38, 4274–4281. https://doi.org/10.1021/ma0501343.

[72] Khasanah, Reddy, K.R., Sato, H., Takahashi, I., Ozaki, Y., 2015. Intermolecular hydrogen bondings in the poly(3-hydroxybutyrate) and chitin blends: their effects on the crystallization behavior and crystal structure of poly(3-hydroxybutyrate). Polym (Guildf) 75, 141–150. https://doi.org/10.1016/j.polymer.2015.08.011.
[73] Gasparyan, K.G., Tyubaeva, P.M., Varyan, I.A., Vetcher, A.A., Popov, A.A., 2023. Assessing the biodegradability of PHB-Based materials with different surface areas: a comparative study on soil exposure of films and electrospun materials. Polym (Basel) 15, 2042. https://doi.org/10.3390/polym15092042.
[74] del Rosario Salazar-Sánchez, M., Campo-Erazo, S.D., Villada-Castillo, H.S., Solanilla-Duque, J.F., 2019. Structural changes of cassava starch and polylactic acid films submitted to biodegradation process. Int J Biol Macromol 129, 442–447. https://doi.org/10.1016/j.ijbiomac.2019.01.187.
[75] Cocca, M., Avolio, R., Gentile, G., Di Pace, E., Errico, M.E., Avella, M., 2015. Amorphized cellulose as filler in biocomposites based on poly(ε-caprolactone). Carbohydr Polym 118, 170–182. https://doi.org/10.1016/j.carbpol.2014.11.024.
[76] Kim, J., Gupta, N.S., Bezek, L.B., Linn, J., Bejagam, K.K., Banerjee, S., et al., 2023. Biodegradation studies of polyhydroxybutyrate and Polyhydroxybutyrate-co-Polyhydroxyvalerate films in soil. Int J Mol Sci 24, 7638. https://doi.org/10.3390/ijms24087638.
[77] Noda, I., Green, P.R., Satkowski, M.M., Schechtman, L.A., 2005. Preparation and properties of a novel class of polyhydroxyalkanoate copolymers. Biomacromolecules 6, 580–586. https://doi.org/10.1021/bm049472m.
[78] Derippe, G., Philip, L., Lemechko, P., Eyheraguibel, B., Meistertzheim, A.-L., Pujo-Pay, M., et al., 2024. Marine biodegradation of tailor-made polyhydroxyalkanoates (PHA) influenced by the chemical structure and associated bacterial communities. J Hazard Mater 462, 132782. https://doi.org/10.1016/j.jhazmat.2023.132782.
[79] Wellen, R.M.R., Rabello, M.S., Fechine, G.J.M., Canedo, E.L., 2013. The melting behaviour of poly(3-hydroxybutyrate) by DSC. Reproducibility study. Polym Test 32, 215–220. https://doi.org/10.1016/j.polymertesting.2012.11.001.
[80] Sedničková, M., Pekařová, S., Kucharczyk, P., Bočkaj, J., Janigová, I., Kleinová, A., et al., 2018. Changes of physical properties of PLA-based blends during early stage of biodegradation in compost. Int J Biol Macromol 113, 434–442. https://doi.org/10.1016/j.ijbiomac.2018.02.078.
[81] Miri, S., Saini, R., Davoodi, S.M., Pulicharla, R., Brar, S.K., Magdouli, S., 2022. Biodegradation of microplastics: better late than never. Chemosphere 286, 131670. https://doi.org/10.1016/j.chemosphere.2021.131670.
[82] Flemming, H.-C., Wingender, J., 2010. The biofilm matrix. Nat Rev Microbiol 8, 623–633. https://doi.org/10.1038/nrmicro2415.
[83] Yuan, J., Ma, J., Sun, Y., Zhou, T., Zhao, Y., Yu, F., 2020. Microbial degradation and other environmental aspects of microplastics/plastics. Sci Total Environ 715, 136968. https://doi.org/10.1016/j.scitotenv.2020.136968.